

# **LiNaK: Multi-Species Apparatus for the Study of Ultracold Quantum Degenerate Mixtures**

by

Ibon Santiago González

Ledo. Physics,

Euskal Herriko Unibertsitatea-University of the Basque Country  
(2008)

Submitted to the Department of Physics  
in partial fulfillment of the requirements for the degree of

Master of Science in Physics

at the

MASSACHUSETTS INSTITUTE OF TECHNOLOGY

June 2012

© Massachusetts Institute of Technology 2012. All rights reserved.

Author .....  
Department of Physics  
May 11, 2012

Certified by .....  
Prof. Martin W. Zwierlein  
Associate Professor  
Thesis Supervisor

Accepted by .....  
Prof. Krishna Rajagopal  
Associate Department Head for Education



# **LiNaK: Multi-Species Apparatus for the Study of Ultracold Quantum Degenerate Mixtures**

by

Ibon Santiago González

Submitted to the Department of Physics  
on May 11, 2012, in partial fulfillment of the  
requirements for the degree of  
Master of Science in Physics

## **Abstract**

This thesis describes the construction of a versatile apparatus to study ultracold quantum mixtures capable of simultaneously cooling fermionic  $^6\text{Li}$  and  $^{40}\text{K}$ , as well as the bosonic  $^{41}\text{K}$ . The main features of the experimental setup are presented, in particular the addition of a new species  $^{23}\text{Na}$ , which has enabled the study of the Bose-Fermi mixture  $^{23}\text{Na}$ - $^{40}\text{K}$ .

Three main experimental benchmarks are outlined: first, the production of a Bose-Einstein Condensate of  $^{41}\text{K}$  is discussed and an evaluation of its properties as a coolant are analysed. Secondly, the creation of a triply degenerate Bose-Fermi-Fermi gas of  $^{41}\text{K}$ - $^{40}\text{K}$ - $^6\text{Li}$  is presented. Simultaneous observation of Pauli Pressure and Bose Condensation in the triply degenerate gas is reported. In addition, interspecies Feshbach resonances between  $^{41}\text{K}$ - $^{40}\text{K}$  and  $^6\text{Li}$ - $^{41}\text{K}$  are observed, opening the way to the study of a strongly interacting isotopic Bose-Fermi mixture of  $^{41}\text{K}$ - $^{40}\text{K}$ , which have similar mass. Thirdly, the creation of a quantum degenerate Bose-Fermi mixture of  $^{23}\text{Na}$ - $^{40}\text{K}$  is discussed and over thirty Feshbach resonances are identified.

Finally, a degenerate  $^{23}\text{Na}$ - $^{40}\text{K}$  Bose-Fermi mixture opens the way to creating fermionic NaK ground state molecules, which are known to be chemically stable and have a larger permanent electric dipole than KRb. This thesis concludes with a review of the molecular properties of NaK and explores the possibilities of bringing Feshbach molecules of NaK into the singlet rovibrational ground state.

Thesis Supervisor: Prof. Martin W. Zwierlein  
Title: Associate Professor



*Lehenik Aitari,  
gero Amari,  
gero nire arrebari,  
ta azkenian, bihotz-bihotzez,  
ene lagun jatorrei.*



## Thanks! Eskerrik Asko!

*Rega as tuas plantas,*

*Ama as tuas rosas.*

*O resto é a sombra*

*De árvores alheias.*

-Fernando Pessoa

This work is dedicated to my family: my *Aita* Josu, my *Ama* Amalia and my sister Jone. Fruit of their love, unconditional support and encouragement is what follows in this thesis. I have incredible parents, they are my constant reference and to them goes my deepest *Eskerrik Asko*; which is the strange, long word we use in Basque to say thank you. In the loving memory of my grandfather *aitxitxe* Valen, the “tinkerer”, I know he would have been proud to see how such a complex apparatus like Fermi 1 was built and produced so much science.

I would like to thank my advisor Martin Zwierlein for giving me the opportunity to work in his group and participate in building two new labs: Fermi 1 and Fermi 2. I also thank him for reading this thesis. Martin’s enthusiasm for what he does is contagious and you can see that throughout the CUA hallway when someone shouts the Eureka analogue of Martin: dyeahh! Martin’s commitment to excellence is a value I share and that I take with me anywhere I go. To him, Danke schön!

My warmest *Mamnoon*, thanks go to our postdoc Peyman Ahmadi, heart and soul and chief director of Fermi 1. I thank him for being a great mentor and friend. Peyman taught me most of what I know of experimental atomic physics. He took the patience to teach me about vacuum, optics and electronics. When problems would be overwhelming, he would divide it into pieces and follow the cartesian method. I have fond memories of building chambers with him, solving electronics puzzles and above all, discussing science and enjoying the beauty of it. Peyman managed to be a superposition of Peymans in many labs. You would open the door of a lab and project the Peyman wavefunction, and you would see him there helping someone. Everybody would ask for him, to the extent that the popular phrase “Is Peyman around?” became

a favourite sentence, along with our lab greeting *Salaam!*. I remember that when oven changes or vacuum catastrophes happened, having Peyman next to us was always a relief, because he knew what the right thing to do was.

Many Eskerrik Asko to my senior graduate student Chen-Hsun Wu for being a partner in the journey of Fermi 1. He once compared the machine to an aeroplane; definitely Cheng not only is an amazing plane engineer but a fantastic pilot as well. He designed and took the lead in building the machine and his endless source of energy and intuition, allowed him to bring the Fermi 1 plane to unexplored scientific islands. And continues so. I cannot but follow the tradition and comment on the witty and refined sense of humour of Mr. Cheng, only accessible to few in very unexpected moments! We have spent together with Peyman many long nights in the initial runs of the machine. It was a pleasure building pieces of Fermi 1 together with him and sharing many exciting discoveries. I remember the adventures of silver-soldering with a torch, playing with alkalis and water (dangerous) and other memorable moments. He taught me how to build lasers and in times of rush and speed, he always took the time to answer questions of any kind. Cheng is a brilliant scientist and more than that, he is also a good friend.

I am also very grateful to the other fantastic of "the fantastic four", Jee Woo (Peter) Park. I remember the shy person that became the lion of Fermi 1. We first worked together in vacuum experiments for many months. We learnt a lot from each other and collaborated in some jobs both in Fermi 1 and Fermi 2. Peyman liked to call us Pat and Mat, referring to the interesting, sometime funny, solutions we came up with. When we started the sodium project, Peter ran the machine and learnt to use it in no time. I thank him for his friendship, kind and calm character and for teaching me so many things.

I would like to thank Wolfgang Ketterle for his inspiring lessons. It was a pleasure to be his teaching assistant and his lectures were always a gift to listen to. Only a superb experimenter like him could give insightful suggestions as to how to approach an experimental problem with our machine. When we had vacuum problems, Wolfgang cared to teach us with his experience. Many thanks to Vladan Vuletic for his

advice in necessary moments.

I thank David Pritchard for his advice and fun Fermi-like problems at PI-student lunches. When I first met him he recited the Gallic Wars opening lines to me: *Gallia est omnis divisa in partes tres...*; to which I can reply, paraphrasing Caesar, ...*Horum omnium fortissimi sunt Vascones*. It was a privilege for me to have met and learnt from such great teachers. To them Eskerrik Asko.

There is a long list of people who I have interacted with in the CUA hallway, who I would like to acknowledge. Most importantly, our fellow mates in the BEC experiments and the new Fermi 2. Ariel Sommer is always a source of inspiration for the great work he does, only comparable to the meticulous and kind Mark Ku. Lawrence Cheuk is a man capable of talking brilliant science while smiling; it's something not commonly seen at MIT. The 3 Musketeers Wasseem Bakr, Tarik Yefsah and Sebastian Will have revolutionized all 3 experiments in very short time. To Tarik, I say merci for his kind words at the right moment and for inviting me to his house-parties. I thank Tout Wang for always interesting discussions and his movie suggestions. I am glad to have become acquainted with Hirokazu Miyake and Marko Cetina; they always gave me good insight and I could borrow some tools from their labs. Many thanks also go to the Cold Atom Walmart BEC 2; in times of lack of Thorlabs stock, BEC 2 would provide us with all necessary waveplates to fill the entire experiment. Late night philosophers Christian Sanner, Wuwei Huang, Aviv Keshet and early morning hard working bird Jon Gillen have been of invaluable help in the success story of Fermi 1. I also want to thank BEC 5 members Yvanna and Niklas for helping us with oven changes and other critical moments in Fermi 1. Special thanks go to Sara Campbell and Thomas Gersdorf. It was a lot of fun to work together and I learnt many things from both of you. I am also grateful to Joanna Keeseberg for making everything work.

Outside the CUA, I would like to thank Prof. Jeff Gore, Prof. Mark Bathe and Prof. Jarillo-Herrero for their encouragement, help and advise. They have always had their office open and talking to them was very enriching for me. I would also like to thank Prof. Krishna Rajagopal and Cathy Modica for their guidance. A big

hug goes to Crystal Nurazura, the best asset of the department; going into her office always brings a big smile to one's face.

Last but not the least, all this would not have been possible without my friends Mona Khazaban, Shamim Nemati, Roberto Galván, Andrew Camacho and Igor Bragado. They are a constant reminder that one should indulge one's passion for science but also remain human. I thank them for getting me out of the lab to enjoy their conversation and I also thank them for their understanding when that did not happen and for all those many moments we have shared together. Eskerrik Asko guztio!

# Contents

<b>1 Overview</b>	<b>15</b>
1.1 Ultracold quantum mixtures as idealized models of Many-Body Physics	15
1.1.1 This thesis . . . . .	17
<b>2 On bosons and fermions</b>	<b>19</b>
2.1 Quantum statistics . . . . .	19
2.1.1 Bosons . . . . .	20
2.1.2 Fermions . . . . .	21
2.2 Properties of Li, K, and Na . . . . .	23
<b>3 The multi-species machine</b>	<b>27</b>
3.1 Vacuum chamber . . . . .	27
3.2 Optics . . . . .	29
<b>4 Cooling and trapping sodium</b>	<b>31</b>
4.1 Essential concepts for cooling, trapping and imaging Na . . . . .	31
4.1.1 The light source: Solid State Laser for Na . . . . .	33
4.1.2 Tools for manipulating light: AOMs and EOMs . . . . .	35
4.1.3 Saturation absorption spectroscopy of Sodium vapour . . . . .	39
4.1.4 MOT, Slower and Repumping and imaging light . . . . .	41
<b>5 Quantum degenerate mixtures</b>	<b>45</b>
5.1 Isotopic Bose-Fermi mixture in a Fermi sea . . . . .	45
5.1.1 Bose Einstein Condensation of $^{41}\text{K}$ . . . . .	45

5.2	Evaporation and sympathetic cooling . . . . .	49
5.2.1	Efficiency of evaporation. Phase space density measurement for different traps . . . . .	50
5.2.2	PSD measurement . . . . .	52
5.2.3	Triply degenerate mixture of $^{41}\text{K}$ , $^{40}\text{K}$ and $^6\text{Li}$ . . . . .	55
5.2.4	Simultaneous observation of Pauli Pressure and Bose-Einstein Condensation . . . . .	59
5.3	Quantum degenerate Bose-Fermi mixture of $^{23}\text{Na}$ and $^{40}\text{K}$ . . . . .	61
5.3.1	Experimental sequence . . . . .	61
5.3.2	Efficiency of evaporation . . . . .	63
<b>6</b>	<b>Interactions: Feshbach resonances</b>	<b>65</b>
6.1	Long-range and short-range interactions . . . . .	66
6.2	Ellastic and Inellastic collisions . . . . .	67
6.3	Feshbach resonances . . . . .	68
6.3.1	Feshbach spectroscopy in $^{23}\text{Na}$ - $^{40}\text{K}$ . . . . .	69
6.3.2	Feshbach spectroscopy in $^{41}\text{K}$ - $^{40}\text{K}$ and $^6\text{Li}$ - $^{41}\text{K}$ . . . . .	72
<b>7</b>	<b>NaK, testbed for ultracold molecular physics</b>	<b>75</b>
7.1	Molecules: Building blocks of nature . . . . .	75
7.1.1	The Molecular Hypothesis . . . . .	77
7.1.2	Molecular spectroscopy: probing molecules . . . . .	79
7.1.3	Experimental methods in Molecular Physics . . . . .	81
7.2	Understanding molecular potentials . . . . .	83
7.2.1	The Born-Oppenheimer approximation . . . . .	84
7.2.2	Model potentials . . . . .	86
7.2.3	Angular momentum in molecules and Hund's cases . . . . .	90
7.2.4	Molecule-Light interactions: Molecular transitions and selection rules . . . . .	92
7.2.5	The Franck-Condon Principle . . . . .	93
7.2.6	Long-range interaction: asymptotic potential . . . . .	96

7.2.7	Example with NaK from known s-wave scattering length and $C_6$	100
7.2.8	Accumulated Phase method	100
7.3	Towards ultracold ground state molecules of NaK	103
7.3.1	Production of molecules via Feshbach resonance	103
7.3.2	STIRAP scheme	103
7.3.3	Reactivity of NaK in the ground state	104



# Chapter 1

## Overview

*...In that Empire, the Art of Cartography attained such Perfection that the map of a single Province occupied the entirety of a City, and the map of the Empire, the entirety of a Province. In time, those Unconscionable Maps no longer satisfied, and the Cartographers Guilds struck a Map of the Empire whose size was that of the Empire, and which coincided point for point with it. The following Generations, who were not so fond of the Study of Cartography as their Forebears had been, saw that that vast Map was Useless...*

-Jorge Luis Borges, “*Del rigor en la ciencia*” (On Exactitude in Science)

### 1.1 Ultracold quantum mixtures as idealized models of Many-Body Physics

Predicting the evolution of a multicomponent system might seem more daunting than the geographer’s task in Borges’ fable. The solutions at hand are either computational calculation or simulation. In the case of an assembly of particles, the computational power required to describe the system increases exponentially with the number of its constituents. A numerical description is thus not an accurate representation of systems with large number of particles and may prevent obtaining the desired accuracy

to explain and understand important phenomena such as high- $T_c$  superconductivity.

Due to the complexity of real materials, an important goal in the study of complex systems, like electrons in solids, is the search for the simplest models that nonetheless describe the physics of interest. Our limited understanding of strongly-correlated electronic systems hinders the development of new materials or even understanding present ones, like high  $T_c$  superconductors. Even simple models that try to capture the underlying physics cannot be solved analytically or numerically, and approximations need to be made. Let us take the simplest pure quantum system we know, N spin-1/2 particles; we would need  $2^N$  coefficients to describe this system and for  $N \geq 50$  this task becomes practically impossible. Quantum simulators -which use one controllable quantum system to investigate the behaviour and properties of another, less accessible one - hold the promise of tackling problems like the latter, which are too demanding for numerical computation [1]. This idea was first introduced by Richard Feynman in 1981 [2] and tremendous advances in isolating and manipulating such simpler quantum systems have been made in the past decades. Most of this progress has been facilitated by the creation of ultracold atoms and quantum gases.

The study of ultracold atoms is a relatively new field that began with the first experimental realization of a Bose-Einstein Condensate (BEC) in 1995 [3], later followed by the creation of the first quantum degenerate fermi gas [4]. Because in cold quantum gases formed by neutral atoms there are no effects of electric charge and crystal impurities, these systems enable the observation of the pure quantum nature of particles and allow realizing fundamental models of condensed matter physics in a fully controllable environment, testing them with the precision of atomic physics. Strong interactions in experiments with cold quantum gases can be created by confining the atoms tightly in optical lattices or by tuning the interaction with so-called *Feshbach resonances*. Feshbach resonances occur when a bound state within a two-body potential is resonant with the energy of a pair of unbound atoms. If the magnetic moment of the bound state and the unbound pair differ, they can be brought into resonance by tuning a magnetic field. The scattering length  $a$ , which is a measure for the interaction strength between atoms, diverges at resonance and it changes the

sign. With Feshbach resonances and optical lattices, the experimenter has at hand tools that facilitate the manipulation of interactions, dimensionality and disorder. By changing these parameters unexplored phases of matter can be realized and studied.

For a long time, the work on ultracold fermionic gases has been limited to homonuclear systems. The addition of a different second fermionic element to create a fermionic heteronuclear system or a bosonic element to create a Bose-Fermi mixture tremendously enriches the system and adds more degrees of tunability. This thesis aims in the direction of constructing an apparatus that will enable the required versatility to undertake such experiments. Finally, another prospect for this kind of systems is to create ground state molecules. Depending on the chosen species, these molecules will be bosonic or fermionic, they can be chemically stable in their ground state and they can exhibit a large dipole-moment enabling more analogies with condensed matter systems, such as artificial crystals, which could be created by applying optical lattice potentials selective to each species. All these examples illustrate the vast possibilities that ultracold mixtures of quantum gases exhibit. Proof of that is the growing number of laboratories that are investigating these nature given gifts.

### 1.1.1 This thesis

Two experimental apparatuses have taken life in our group during my time at the CUA and I had the privilege to be involved in the construction of both of them. During my first year we built the Fermi 1's LiNaK machine and our first Bose-Einstein Condensate of  $^{41}\text{K}$  saw light (literally) in a record time of one year after. A second project started in parallel after this and it was coined as Fermi 2, in order to study  $^6\text{Li}$ - $^{40}\text{K}$  mixtures using a 2D MOT. Together with Jee Woo Park, Sara Campbell and Vinay Rameshesh we built a machine that was later replaced by the Fermi 2 microscope project. In Fermi1 the ability to use naturally abundant isotopes of potassium, as well as lithium allowed us to study diverse combinations of Bose-Fermi or Fermi-Fermi mixtures. Shortly after our first BEC, we were able to use it as a fridge for our fermionic species and formed a triply degenerate gas. We observed multiple heteronuclear Feshbach resonances, in particular a wide s-wave resonance

for the combination  $^{41}\text{K}$ - $^{40}\text{K}$ . We also characterized the efficiency of  $^{41}\text{K}$  as a coolant and provided evidence for Pauli pressure as we cooled the fermionic species  $^{40}\text{K}$  and  $^6\text{Li}$ .

After the big success of obtaining a triply degenerate quantum mixture in Fermi 1, I undertook the stimulating job of adding sodium to our LiNaK machine and setting up the Na optical table; with the invaluable help of my co-workers. One month after the setup was completed, we obtained the Na MOT and shortly after, our Bose-Einstein Condensate of sodium. With this, we had the best available coolant and our next step was to study how well it could cool  $^{40}\text{K}$ . This triggered the discovery of up to thirty Feshbach resonances for the new Bose-Fermi mixture and with some broad resonances at hand, Fermi 1 has recently created NaK molecules, opening up the possibility of generating fermionic dipolar ground state molecules, where dipolar interactions would set the dominant energy scale.

This thesis is outlined in the following way:

- **Chapter 2** introduces the atomic species that LiNaK is based on and discusses some fundamental concepts of quantum statistics.
- **Chapter 3** describes the experimental apparatus: the vacuum chamber and general optical setup.
- **Chapter 4** explains the Na optical table setup in detail.
- **Chapter 5** describes the creation of a BEC of  $^{41}\text{K}$ , as well as its use as a coolant. Phase-Space density is calculated and is used to measure the efficiency of evaporation. The triply degenerate quantum gas is explained, as well as the use of sodium as a coolant for potassium.
- **Chapter 6** is an introduction to interactions and very basic scattering theory. Feshbach resonances are explained and experimental measurements are listed.
- **Chapter 7** is a primer in molecular physics in the context of the creation of NaK ground state molecules.

# Chapter 2

## On bosons and fermions

### 2.1 Quantum statistics

When describing the behaviour of ultracold dilute gases, quantum mechanics takes central stage. A feature that separates classical from quantum mechanics is that of *distinguishable* particles. If two quantum mechanical particles are in the same internal state, we say they are *indistinguishable*. If their wavefunctions overlap it is impossible to determine after the time evolution of the system, which particle originated from where. This concept of indistinguishability is what gives rise to the fundamental difference between *classical* and *quantum statistics*.

On the basis of symmetry of the system all of the light and matter in the universe can be divided into two categories: bosons and fermions. They are distinguished from one another by their quantum mechanical spins. As such, quantum statistics is further divided into the following two classes: *Bose-Einstein* and *Fermi-Dirac* statistics. This division is based on the *Pauli Principle*, which extended to N number of particle states that:

The wave function of a set of N indistinguishable particles is completely symmetric and remains unchanged upon exchanging two arbitrary particles. In this case, these particles are classified as *bosons*. If the wavefunction is completely antisymmetric, it changes sign when two particles are

exchanged. In this case the particles are named *fermions*

The *spin-statistics* theorem, derived by Wolfgang Pauli [5], relates quantum statistics to the spin of the particles. All particles with integer spin or zero are bosons, whereas particles with half-integer spin are fermions. Consequences of quantum statistics can be seen in different Helium isotopes: electron structure of fermionic  ${}^3\text{He}$  and bosonic  ${}^4\text{He}$  are exactly the same, but the number of neutrons is different, which leads to a different quantum statistics [6]. Another example is the one of fermionic  ${}^{40}\text{K}$  and bosonic  ${}^{41}\text{K}$ , which will be discussed in this thesis.

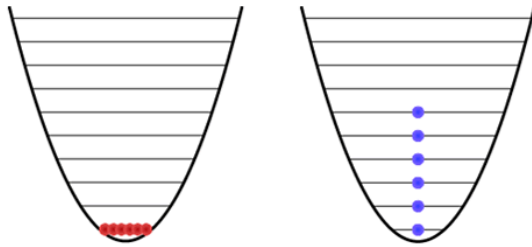


Figure 2-1: A Bose-Einstein Condensate (Left) and a Fermi sea (right) in a harmonic trap.

### 2.1.1 Bosons

The possible many-body wavefunctions of non-interacting bosons are given by symmetric combinations of single-particle eigenstates. The ground state is the state where all particles occupy the same single-particle ground state  $|0\rangle$  with energy  $E_0$ . A macroscopic occupation of a single quantum state gives rise to a new state of matter known as *Bose-Einstein condensate (BEC)*. It was predicted for non-interacting particles by Albert Einstein and S.N. Bose in 1925 and was observed in dilute gases for the first time in 1995 [3].

For finite temperature  $T$ , the occupation of the single-particle eigenstates is given by the Bose-Einstein distribution, where  $\epsilon$  is the eigenenergy.

$$N(\epsilon) = \frac{1}{\exp \frac{\epsilon - \mu}{k_B T} - 1} \quad (2.1)$$

where  $\mu$  represents the chemical potential. There exists a critical temperature  $T_c$  below which the ground state occupation  $N_0$  becomes macroscopic. For the particular case of interest, which is that of 3D harmonic trap, under the semi-classical approximation the condensate fraction  $N_0/N$  is given by:

$$\frac{N_0(T)}{N} = 1 - \left( \frac{T}{T_c} \right)^3 \quad (2.2)$$

imposing a null population of the ground state  $N_0 = 0$  and solving an integral as in [7], we obtain the BEC critical temperature:

$$T_c = \left( \frac{N}{\zeta(3)} \right)^{1/3} \frac{\hbar \bar{\omega}}{k_B} \quad (2.3)$$

The two relevant energy scales for such system are the thermal excitation energy and the mean levels of separation. For our experimental apparatus the typical trap frequency for  $^{41}\text{K}$  is  $\bar{\omega} = 2\pi 380$  MHz, which corresponds to a mean spacing of 18 nK, which fulfils the requirement for the semi-classical approximation  $k_b T_c \gg \hbar \omega$ .

The onset of Bose-Einstein Condensation is characterized by the bimodality of the cloud in time-of-flight images (TOF): an elliptical core is the condensed atoms, surrounded by a round homogeneous background thermal cloud.,

In our experiment we have three bosonic species:  $^{39}\text{K}$ ,  $^{41}\text{K}$  and  $^{23}\text{Na}$ <sup>1</sup>.

### 2.1.2 Fermions

Fermions have half integer spin. Everything surrounding us is made of fermions, that is, electrons, protons and neutrons. Any neutral atom with uneven number of neutrons is a fermion. An important concept is that of a *degenerate fermi gas*, in which all energy states below a critical value  $E_F$ , the Fermi energy, are filled. By the Pauli

---

<sup>1</sup>Note that for alkalis, which have a single valence electron and hence an odd number of them; an odd A number translates into an even number of fermions ( $e^-$ ,  $p^+$  and  $n^0$ ). Hence, neutral atoms with odd A number are bosons, whereas even number are fermions

principle, no quantum state can be occupied by more than one fermion with identical properties. Thus a Fermi gas, unlike a Bose gas, is prohibited from condensing into a Bose-Einstein condensate but instead will form a *Fermi sea*. The atoms will occupy the  $N$  lowest energy states by exactly one fermion per state. Important examples are that of the electronic structure of atoms, where because of the Pauli exclusion, not all electrons collapse onto the 1s energy state. In the same way, conductance electrons, because of the same principle, can give rise to insulating or metallic materials.

Non-interacting fermions in thermal equilibrium follow the *Fermi-Dirac distribution*, which for the single-particle eigenstate of the hamiltonian with energy  $\epsilon$  is given by:

$$f(\epsilon) = \frac{1}{e^{\frac{\epsilon-\mu}{k_B T}} + 1} = \frac{1}{z^{-1} e^{\frac{\epsilon}{k_B T}} + 1} \quad (2.4)$$

where  $\mu$  is the chemical potential which controls the particle number  $N$  and  $z$  is a the fugacity parameter. This distribution function in the limit of  $T = 0$  becomes the heaviside function  $f(\epsilon) = \theta(E_F - \epsilon)$

For a 3D harmonic trap we can solve the integrals as in [8] and obtain the following important thermodynamic variables that will be widely used in this thesis: The Fermi temperature,

$$T_F = \frac{E_F}{k_B} = \frac{\hbar\bar{\omega}}{k_B} (6N)^{1/3} \quad (2.5)$$

and a useful relationship between the fugacity and the reduced temperature  $T/T_F$ :

$$Li_3(-z) = -\frac{1}{6(T/T_F)^3} \quad (2.6)$$

where  $Li_3$  is the polylogarithm. More relations and the relevant integrated density distribution are given in [8].

## 2.2 Properties of Li, K, and Na

The alkali atoms we use have bosonic and fermionic isotopes. Here is a list of them and their natural abundances:

Isotope	Quantum statistics	Natural abundance
$^6\text{Li}$	fermion	7.5%
$^{39}\text{K}$	boson	93.26%
$^{40}\text{K}$	fermion	0.012%
$^{41}\text{K}$	boson	6.73%
$^{23}\text{Na}$	boson	100%

Table 2.1: Used alkalis in the LiNaK machine, the quantum statistics they obey and their natural abundance.

The underlying idea of laser cooling and trapping is to use our knowledge about the internal structure of atoms to manipulate their external degrees of freedom. It is therefore necessary to know these properties thoroughly. All our experiments are done with alkali atoms, which all have an unpaired electron in the S shell. The first excited state is of the form  $n^2P_J$  and is split by spin-orbit ( $\vec{L} \cdot \vec{S}$ ) coupling into  $J=1/2$  and  $J=3/2$  states. We will be concerned only with the  $n^2P_{3/2}$  state, which connects to the ground state by the  $D_2$  line. The wavelength corresponding to this transition is 671 nm for lithium, 589 nm for sodium and 767 nm for potassium. Because these wavelengths lie in the visible, they are attractive for laser cooling and trapping. Further splittings are due to the coupling between the electron and the nuclear spin. At low magnetic fields, the good quantum number is  $\vec{F} = \vec{I} + \vec{J}$  and its projection along the quantization axis,  $m_F$ . The values for the nuclear spin are  $I=1$  in  $^6\text{Li}$ ,  $I=3/2$  in  $^{23}\text{Na}$  and  $I=4$  in  $^{40}\text{K}$ . The hyperfine splitting of the ground state is 228 MHz in  $^6\text{Li}$ , 1.77 GHz in  $^{23}\text{Na}$  and 1286 MHz in  $^{40}\text{K}$ .

Relevant optical and magnetic properties of these alkalis can be found in the following sources: potassium [9], sodium (Alkali D Line Data by Daniel Steck) and lithium [10]. For the reader new to the art of laser, cooling and trapping, a nice introduction can be found in William Phillip's Nobel Prize lecture [11].

Below, the hyperfine structure and used transitions are depicted for lithium and

potassium. Sodium and other potassium isotopes are discussed later in the thesis.

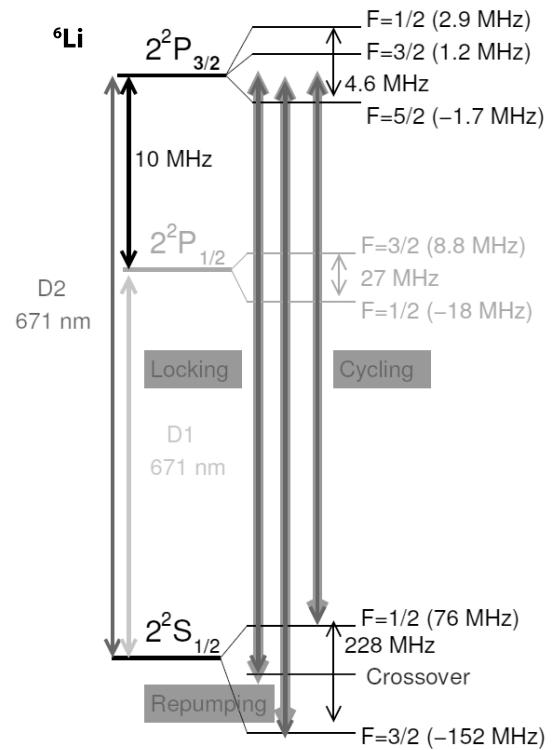


Figure 2-2: Hyperfine structure and transitions for  ${}^6\text{Li}$ .

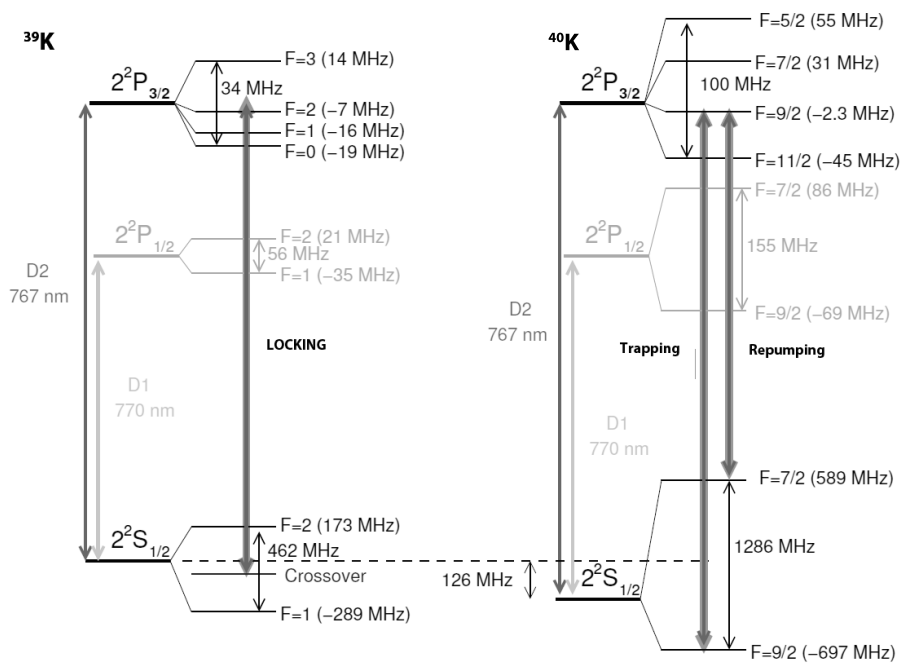


Figure 2-3: Hyperfine structure and transitions for  $^{39}\text{K}$  and  $^{40}\text{K}$ . This figure was modified from [12]



# Chapter 3

## The multi-species machine

*In this chapter I will describe the main features of the new apparatus LiNaK (Fermi 1) for creating quantum mixtures. Building of this apparatus was carried out by Cheng Hsun Wu, Dr. Peyman Ahmadi and the author, later joining Jee Woo Park and with the invaluable help of undergraduate students Sara Campbell, Caroline Figgat and Kevin Fisher. It remains as one of the most versatile machines in the field of ultracold atoms.*

### 3.1 Vacuum chamber

The Fermi 1 LiNaK apparatus belongs to a new generation of ultracold atom experiments at MIT. It is inspired by previous setups and incorporates the most advantageous features of its predecessors.

The apparatus consists of two independent Zeeman slowers, optimized for  ${}^6\text{Li}/{}^{23}\text{Na}$  and all three K isotopes. The oven is designed as a source for two species and it contains two cups where each of the source ampules are placed and heated. The favorable mass ratio between sodium and lithium allows for simultaneous Zeeman slowing of both species, resulting in a very bright atomic beam. We heat the K cup up to  $190^\circ\text{C}$  and the Li/Na cups are run at  $300^\circ\text{C}$ . The vapour is sprayed out from a nozzle in  $2\pi$  solid angle into a six-way cross where we had a cold plate. The cold plate serves to collect most of the sodium/lithium that sprayed out of the nozzle. It

is a simple copper plate that can be externally cooled. The beam shutter is placed immediately after the cold plate. It is a simple “flag” made out of steel with a tapped hole in the blank. An actuator controls whether the flag is blocking the atomic beam or not. As the atomic beam passes through the shutter it enters the Zeeman slower where atoms are slowed down to  $\approx K$  (30 m/s).

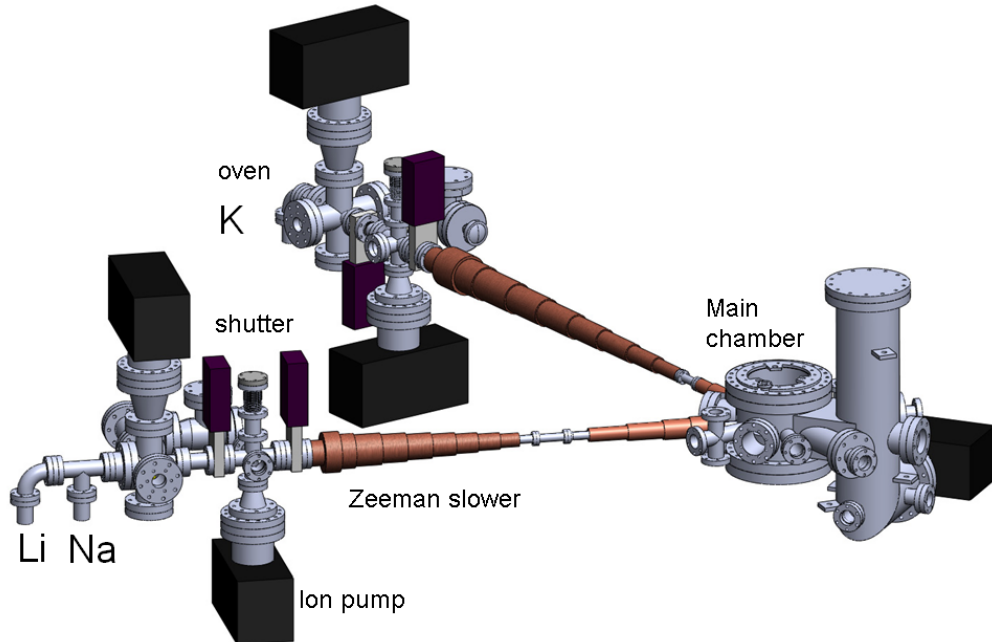


Figure 3-1: Two independent Zeeman slowers for lithium/sodium and potassium, allowing us to simultaneously load large samples of each of the three atomic species directly into a UHV chamber. Atoms are cooled, trapped and imaged in the main chamber.

These cold atoms are then captured by the Magneto-Optical trap located in the main vacuum chamber. The main chamber combines the robustness of a stainless steel chamber with the excellent optical access of glass cell experiments. The main chamber features five inserted “bucket” windows, two of them 4” in diameter and only 0.5” away from the atoms. It provides optical access for slowing, trapping and imaging from six sides.

Perfect thermal isolation between our atomic gases and the stainless steel walls

surrounding them is necessary in ultracold atom experiments. Transfer of energy from the walls to the gas sample can take place through residual gas molecules. That is why we need to work in ultra high vacuum conditions (UHV is defined below  $10^{-9}$ Torr). In order to achieve pressures as low as  $10^{-12}$ Torr, a proper “bake-out” is needed, whereby residual gases ( $H_2$ , hydrocarbons,  $CO_2$ ,  $H_2O$ ...) are out-gassed and pumped out of the chamber. In this process, we used three kinds of pumps: rotary pumps, turbo pumps and ion pumps. Up to 5 ion pumps maintain the UHV in the chamber. On top of this, titanium sublimation pumps make the chamber itself act as a getter (mostly for  $H_2$ ) by adding a layer of Ti on the surfaces. Separating the chamber from the oven there are two MDC gate-valves and one VAT manual valve that allow complete isolation of the main chamber from the source and facilitates an easy oven change.

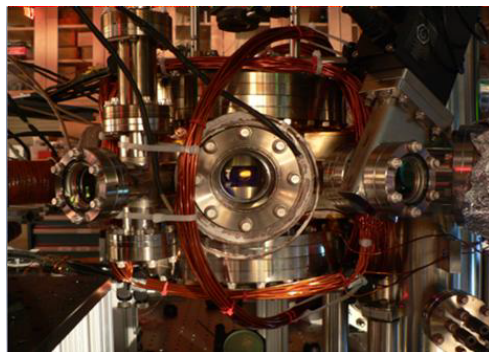


Figure 3-2: Main UHV vacuum chamber (Science chamber) where Magneto-Optical Trapping (MOT) of  $^{40}K$ ,  $^{41}K$ ,  $^{39}K$ ,  $^6Li$  and  $^{23}Na$  has been achieved.

## 3.2 Optics

Two laser tables address the host of different alkali atoms that are cooled and trapped in our experiment. On one of the tables, the potassium laser systems consists of a home-made grating-stabilized diode master laser (767 nm), 4 slave lasers and 4 tapered amplifiers. Making use of many optical and acusto-optical tools, the necessary light to cool, trap and image all 3 isotopes of K is generated and transported via

optical fibers to the experimental table. Next to it, the lithium setup consists of a Toptica DL Pro (671 nm) and tapered amplifier BoosTA, as well as 2 slave diode lasers. Both laser setups make use of doppler-free saturation spectroscopy to lock to the absorption lines (we usually lock to the  $D_2$  crossover resonance for the most abundant isotope in the absorption cell, i.e.  $^{39}\text{K}$  and  $^6\text{Li}$ ).

On the second table, the sodium laser system is setup, as well as a Ti:Saph CW Ring laser for spectroscopy. The sodium laser setup will be treated in the next chapter separately.

Below we see fluorescence from Magneto-Optical traps that have been realized with this apparatus.

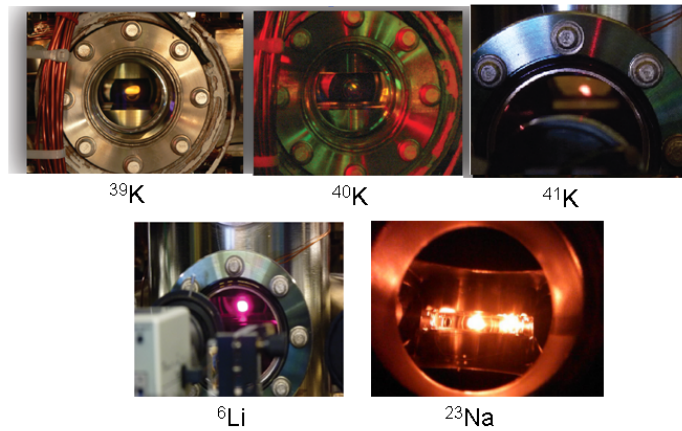


Figure 3-3: MOTs of all 4 species

# Chapter 4

## Cooling and trapping sodium

*In this chapter we present a laser system which creates the slowing, trapping and imaging light of  $^{23}\text{Na}$ . The natural choice for a laser source has traditionally been a dye laser; however, for the first time for laser cooling of Na, we have adopted a solid-state based laser that produces the necessary power (maximum of 2W) of the yellow transition line of sodium (589nm). This setup is based on previous work in BEC1[13]; a bit more compact and without the hassle of dye lasers. The optical setup may be divided into three different sections: the one dedicated to spectroscopy, another one for trapping and slowing light and the last one dedicated to imaging. We begin by introducing the basic properties of sodium and a description of the laser source.*

### 4.1 Essential concepts for cooling, trapping and imaging Na

The slowing and trapping of sodium involves several laser frequencies. These are manipulated on the optical table by means of acousto-optical modulators (AOMs), electro-optical modulators (EOMs) and a series of optical elements. The diagram below shows the interesting part of the energy level diagram of  $^{23}\text{Na}$  relevant to our work.

A sodium atom in the ground state has a single valence electron in the  $3S_{1/2}$

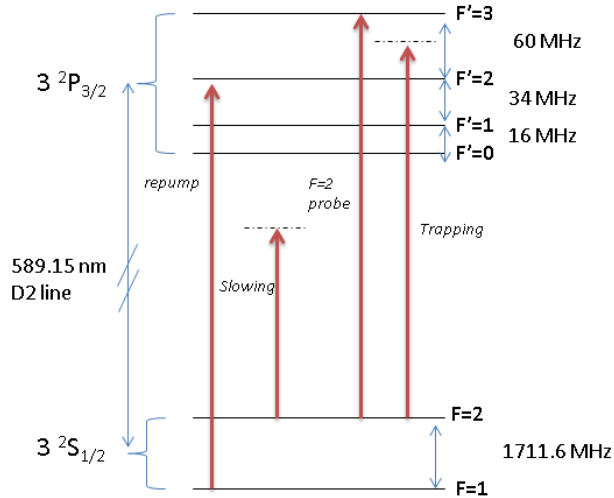


Figure 4-1: Level diagram for  $^{23}\text{Na}$  showing the hyperfine structure for the  $3S_{1/2}$  ground state and the  $3P_{3/2}$  excited state. Shown is the cycling transition  $|F = 2\rangle \rightarrow |F' = 3\rangle$ .  $F=1$  imaging and repumping light is resonant with the  $|F = 1\rangle \rightarrow |F' = 2\rangle$  transition and hence, blue detuned 1.71 GHz from the cycling transition. The slower light is red-detuned (roughly 1 GHz) from the cycling transition.

configuration. With a nuclear spin of  $I=3/2$ , the two ground state hyperfine manifolds have total spin  $F=1$  and  $F=2$ , split by a hyperfine frequency of 1.71 GHz. The ground state has two strong absorption lines from transitions to the excited 3P state known as *the sodium doublet*. The D1 line at 589.6 nm for excitation to the  $3P_{1/2}$  state, and the D2 line at 589.15 nm for the excitation to the  $3P_{3/2}$  state. We lock our laser onto the D2 line. The excited state has a natural lifetime of 16 ns (linewidth of 10 MHz) on the  $|F = 2\rangle \rightarrow |F' = 3\rangle$  transition, and has four hyperfine manifolds with total spin ranging from  $F=0$  to  $F=3$ .

In order to laser cool, a *cycling transition* is required, in which a Na atom returns to the same ground state after scattering a photon. Such a transition is the  $3S_{1/2}|F = 2\rangle \rightarrow 3P_{3/2}|F' = 3\rangle$  transition. There is an additional effect one needs to consider in laser cooling; occasionally light scattering will transfer an atom from the  $|F' = 2\rangle$  state to the  $|F = 1\rangle$  state. A *repumping* beam fixes this, by exciting atoms from the  $F = 1$  manifold to transfer them back. In addition, sodium atoms need to be slowed

down along the Zeeman slower before they reach the vacuum chamber. Atoms are exposed to red-detuned light from the cycling transition and because of the Doppler shift, only a short range of velocities will be in resonance. This is achieved by detuning light 1 GHz from the cycling transition to generate *slowing light*.

#### 4.1.1 The light source: Solid State Laser for Na

Alkali metals like sodium have simple optical properties due to the presence of a single valance electron. This makes alkali atoms amenable to laser cooling by providing strong optical transitions, where lasers are available. Reaching the transition line of Sodium at 589 nm (the well-known “sodium doublet”) typically requires a dye laser system. Although well-mastered in the CUA and other atomic physics research groups, dye laser systems are expensive and notoriously difficult to maintain and operate. As a result, other alkalis such as Rubidium or Cesium, whose resonances can be addressed using cheaper and more user-friendly laser diodes, have become more attractive for spectroscopy or atomic physics applications. This picture has dramatically changed with recent advances in nonlinear frequency conversion and this has allowed our group to adopt a solid-state based 589 nm yellow light source.

The setup consists of a polarization maintaining optical amplifier for amplification of a narrowband CW signal from an external 1178 nm grating stabilized diode laser (TOPTICA DL Pro) with a subsequent frequency doubling of the amplified signal in a Second Harmonic Generation (SHG) module. It consists of a Visible Raman Fiber Amplifier Module and Fiber laser pump module (MBP Photonics). The pump light from the pump module is guided to the amplifier by a polarization maintaining pump delivery optical fiber. The pump module allows monitoring of the Raman Fiber Amplifier signals via the RFA monitor cable. It also provides an active power stabilization of the SHG output power and temperature stabilization of the SHG crystal. The optimal temperature may be slightly different at different pump laser diode currents. Practically, one should optimize the SHG temperature at a certain reference current, for example at 4 A, then keep the temperature setting for the whole current range and record this information to avoid power drifts in the setup.

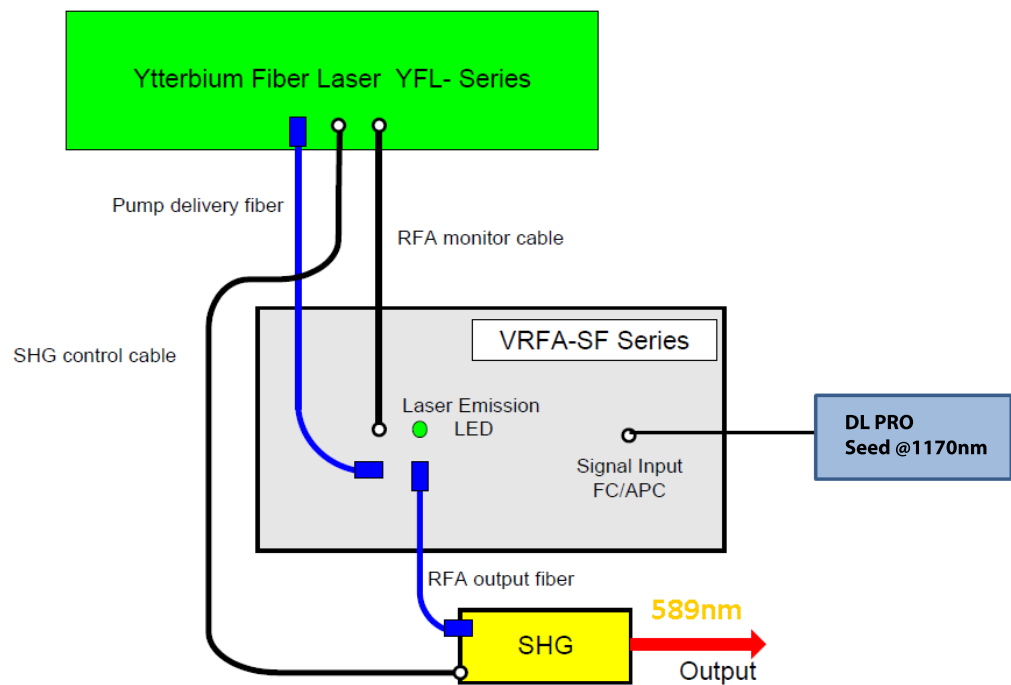


Figure 4-2: Diagram of Raman Fiber Amplifier (MPBC VRFA-SF series) pumped by Ytterbium Fiber Laser (MPBC YFL series). The seed laser is a 1178nm TOPTICA DL Pro grating stabilized diode laser.

Two principles govern this 589nm light generation: amplification and second harmonic generation. On the one hand, the tunable grating stabilized DL Probe provides roughly 20mW and this is further amplified in the Raman Amplifier module. *Stimulated Raman Scattering (SRS)* takes place and the lower frequency seed induces the inelastic scattering of a higher frequency 'pump' photons in an optical medium in the nonlinear regime (in this case, an optical fiber). As a consequence the pump photons that undergo inelastic scattering with the glass molecules of the fibre core, excite vibrational states of the medium and create 'optical phonons', which divert part of the photon energy so that the pump photons are shifted to longer wavelengths, known as the *Stokes shift*. After the all-optical amplification to  $\approx 10$  W of 1178 nm, in a second step, the signal is frequency doubled after going through a Lithium Triborate (LBO) crystal which is mounted inside a temperature controlled oven. The system can produce up to 1.8 W of 589nm yellow light.

Raman-fiber-amplifier-based 589 nm sources were developed by Dr. Yan Feng et al. and have attracted attention in astrophotonics as a reliable and compact source for laser guide star. The laser beam is projected at approximately 100 km in the mesosphere, producing laser guide stars by excitation of mesospheric sodium atoms. Introducing this laser in the ultracold atom community is relevant, given the importance of sodium as one of the best coolants among alkali atoms. Our laser was developed by the MPBC<sup>1</sup>. Further discussion on the development of this laser can be found in the literature by Feng et al [14].

#### 4.1.2 Tools for manipulating light: AOMs and EOMs

In addition to a light source, it is necessary to have control over power, frequency, size and direction of the laser beam. To this end, several optical components are used, such as: *polarizing beam-splitters* (splits light into beams of differing polarization),  $\lambda/4$  and  $\lambda/2$  *waveplates* (retarders that alter the polarization state of the beam by creating a phase shift), mirrors (-A coated for 589nm), shutters (Uniblitz, millisecond switching time) and all sorts of lenses to focus or collimate the light. CVI Melles Griot

---

<sup>1</sup>MPB Communications Inc.; Montral, Quebec

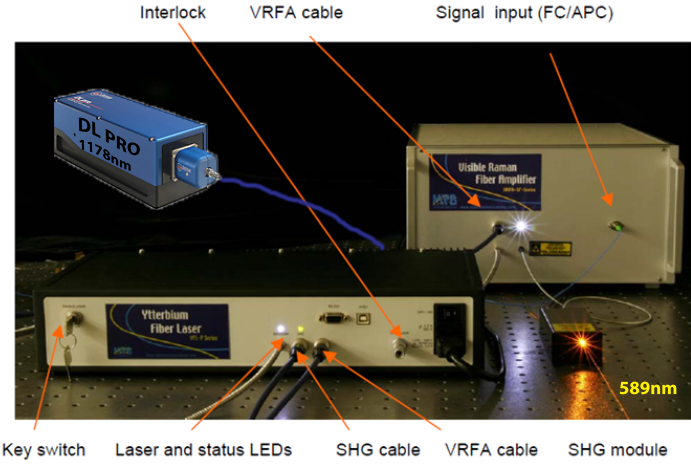


Figure 4-3: Photograph of the Raman Fiber Amplifier, Ytterbium Fiber laser, Seed diode laser and the Second Harmonic Generator (SHG) head.

provides a comprehensive technical guide to optical components [15].

The interaction between sound waves and light is a broad and fascinating field of study, appropriately named Acousto-optics. This is the main physical principle that we use in our experiment to shift the frequency of our light beams. Radiofrequency is generated in home-built or commercially available drivers (IntraAction Inc.) and this power is transformed into sound waves inside a Tellurium Dioxide  $\text{TeO}_2$  crystal via a piezoelectric transducer that is attached to it. The travelling sound wave exchanges energy and momentum with the photons traversing the crystal. This effect can be explained as *Bragg diffraction* of photons from a crystal lattice . An incident laser beam passing through the crystal will diffract the laser beam into several orders. The first order beam has normally the highest efficiency. Its angular position is linearly proportional to the acoustic frequency, so that the higher the frequency, the larger the diffracted angle. In the diagrams below two common configurations of AOMs that overcome beam steering are presented: *double-pass* and *Tandem*. There are tricks that can speed up the optimization of an AOM; however one can always make use of a photodiode and maximize the desired diffraction order, while rotating the AOM and adjusting its height. A key signal is the reduction of light intensity of the

non-diffracted zeroth order beam. A general discussion on Acusto-optical theory and devices can be found in the book by A. Korpel [16].

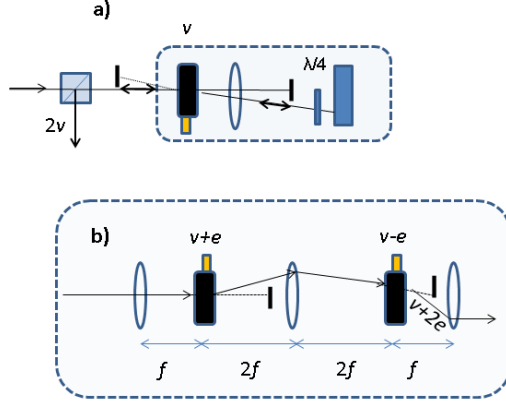


Figure 4-4: Some AOM configurations used in the experiment. In a) *double-passed* AOM shifts the beam frequency  $v$  in the first pass. The beam is retroreflected and shifted again for a total shift of  $2v$ . The output exhibits no steering of the beam. In b) the *TANDEM* configuration, one AOM is driven at a frequency  $v+e$  and the other one at  $v-e$ . Gives a total shift of  $2e$ , allowing fast small frequency shifts without steering the beam.

**BRIMROSE 1.77GHz AOM (Repumping beam)** Of particular difficulty is the setup of the modulator required for generating the repumping and imaging lights for the  $|F = 1\rangle \rightarrow |F' = 2\rangle$  transition. This is done using a high-frequency acousto-optic modulator (TEF-1700-100-589, Brimrose Corp). The BRIMROSE AOM is placed on a translational and rotational stage that allows fine tuning for optimization of the diffraction efficiency ( $\approx 25\%$ ). A  $f=100\text{mm}$  lens was necessary to focus the beam into the transducer of the AOM ( $75\mu\text{m}$ ). The beam has to be linearly polarized for maximum efficiency. The driver that powers this AOM is home-built and generates less than 1W of 1.77 GHz.

**Electro-Optic Modulators and EOM Driver** As opposed to an AOM, which changes frequency spatially by splitting the main beam into different orders, an EOM adds frequency components in the time domain. This is the electro-optic effect, known

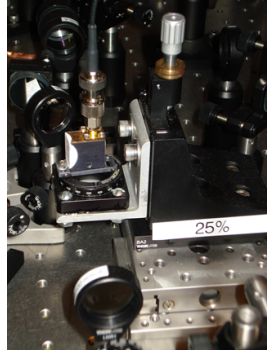


Figure 4-5: Brimrose high-frequency acusto-optic modulator set on a x-y-z translational stage.

as Pockels effect, where the refractive index of a medium is modified in proportion to the applied electric field strength. The most important materials of this type are crystal materials such as lithium niobate ( $\text{LiNbO}_3$ ).

When building an EOM, the crystal is placed next to an inductor made from about 10 loops of wire and a capacitor made from two pieces of copper solder wick on either side of the crystal. These are wired in a series LC circuit and RF power from an EOM driver is coupled to it through a BNC cable.

The EOM driver is designed to produce up to 5W radio frequency signal. To generate a 1.7GHz signal, we create a  $x80$  frequency multiplier using a phase detector with a loop filter (PDF) out of RF Bay Inc. components. The driver box has an attenuator to prevent damaging the amplifier since an input power of  $+1\text{dBm}$  is not to be exceeded.

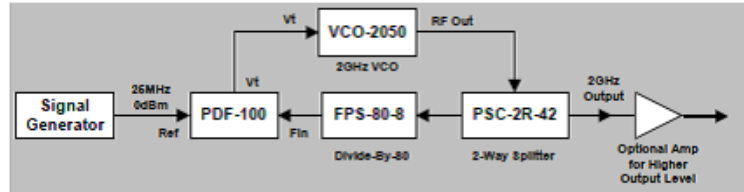


Figure 4-6: Schematics of phase detector loop filter used to drive the EOM

RF Bay Part Number	Description
PDF-100	3-300MHz Phase Detetor with Loop Filter
FPS-80-8	0.8-8.0 GHz Divide by 80 Prescaler
VCO-2050	1950-2150MHz Voltage Controlled Oscillator
PSC-2R-42	DC-4200MHz Splitter
MiniCircuit ZHL-5W-26-S+	RF Amplifier

Table 4.1: List of necessary parts for building an EOM driver

The two inputs of the phase detector are the reference input and the feedback from the VCO after dividing the signal by 80. The PD output controls the input voltage to the VCO, such that the phase difference between the two inputs is held constant, making it a negative feedback system.

#### 4.1.3 Saturation absorption spectroscopy of Sodium vapour

We lock the laser beam 142 MHz below our primary trapping resonance (being the  $F = 2, m_F = 2$  to  $F' = 3, m_F = 3$  transition). For that, the laser beam goes through a double pass AOM first and then into the spectroscopy area.

An absorption cell is used for saturation-absorption spectroscopy; the cell is kept at a temperature of 230 °C. Coating of the cell was a major issue, and the problem was solved by placing the cell inside a cylinder with different layers of heating bands. The wrapping was done in such a way as to generate a temperature gradient, with the side windows being hotter than the middle. This strategy proved not to coat the cell as much and allowed proper absorption spectroscopy.

In an absorption spectrum of Na vapour at  $\approx 200^0$  C, the atomic transitions are broadened to several GHz by the Doppler effect. Saturated absorption spectroscopy, first developed by T.Haensch and Schawlow [17], overcomes this problem by selecting only a specific velocity class of atoms and thus providing a Doppler free signal that has a width closer to the natural linewidth ( $\Gamma \approx 2\pi10\text{MHz}$ ). The experimental setup consists of two overlapping counterpropagating beams, called pump and probe, which interact with the Na atoms in the cell. The probe beam is detected on the photodiode which measures its absorption by the vapor.

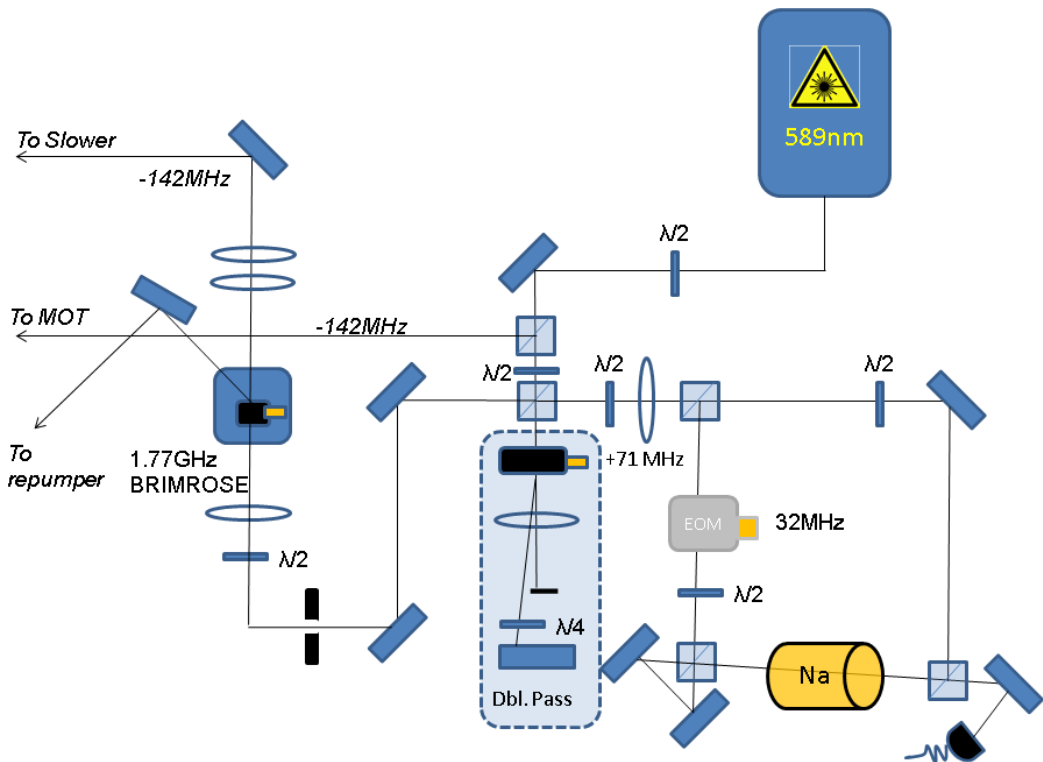


Figure 4-7: Laser source and spectroscopy area. A Brimrose AOM is used to shift the frequency 1.77 GHz to provide repumping and imaging light

In order to stabilize the laser to a reference frequency an electro-optic modulator is used to generate an error signal. The resonant frequency is 32MHz. The voltage across the capacitor oscillates and produces an oscillating electric field inside the crystal. In turn, the index of refraction of the light will oscillate in time. Therefore, the phase change that the laser light acquires will also oscillate in time. We chose to modulate the probe beam. After some signal processing we get an anti-symmetric error signal that we will be able to lock to (see Fig. 4-8).

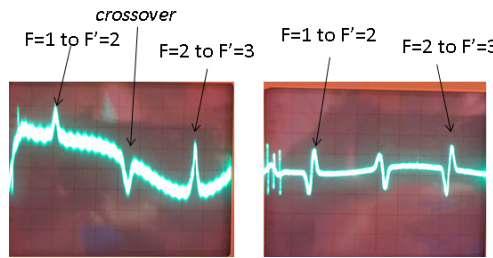


Figure 4-8: Absortion signal (left) and dispersion signal (right)

#### 4.1.4 MOT, Slower and Repumping and imaging light

In the following two diagrams the generation of MOT light, repumper beams and slower beams are depicted. Before each fiber there is a clean-up process to avoid fluctuations in polarization, since this would compromise the fiber-coupling to a polarization maintaining fiber. The imaging beams are taken from the zeroth order of the repumper beam and from the zeroth order of the MOT beam and combined and frequency shifted to give  $F=1$  and  $F=2$  imaging light. These are combined in a cube and separated into imaging-x and imaging-y, which are two different imaging directions.

In the table below, key frequencies read on AOM drivers that change throughout the experimental sequence are given. Other frequencies that remain always constant are listed on the diagram.

	Imaging	Optical Pumping	MOT
F=1 Imaging	88.3 MHz	111.3 MHz	100 MHz
TANDEM 1st AOM	199 MHz	212.1 MHz	-
TANDEM 2nd AOM	200 MHz	187.7 MHz	-

Table 4.2: Key frequencies throughout experimental sequence read off AOM drivers.

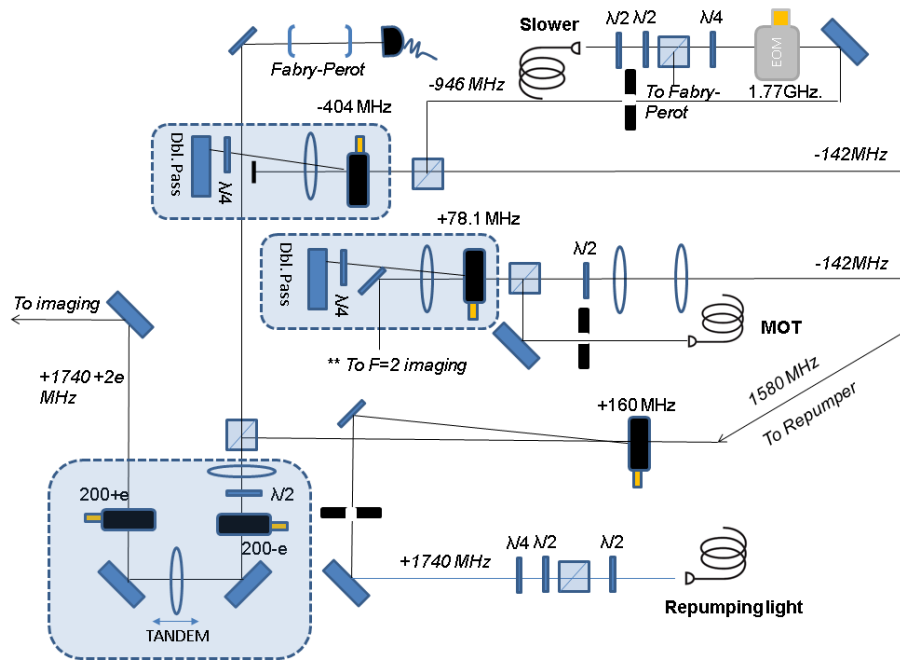


Figure 4-9: MOT light, repumper and slower lights

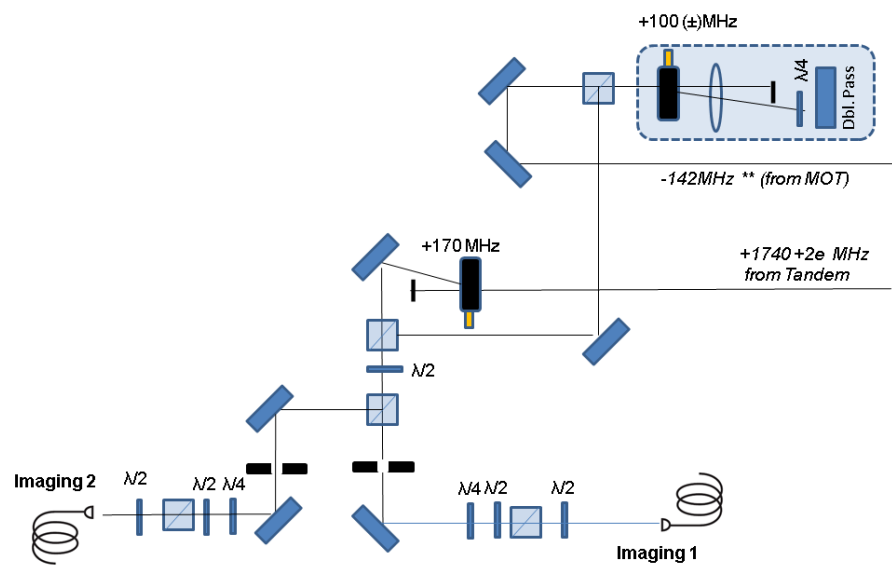


Figure 4-10: Imaging light diagram.



# Chapter 5

## Quantum degenerate mixtures

### 5.1 Isotopic Bose-Fermi mixture in a Fermi sea

In this section we review the creation of a Bose-Einstein Condensate of  $^{41}\text{K}$  and study its properties as a coolant. We also report on the generation of a triply degenerate quantum gas of  $^{41}\text{K}$ ,  $^{40}\text{K}$  and  $^6\text{Li}$ . Density profiles provide information about properties of the clouds and allow us to observe different quantum statistics in the case of fermionic  $^6\text{Li}$  and  $^{40}\text{K}$  and bosonic  $^{41}\text{K}$ . We show that  $^{41}\text{K}$  is an efficient coolant by measuring the phase-space-density (PSD) evolution while  $^{41}\text{K}$  is evaporated. Finally, we simultaneously observe Pauli pressure and Bose-Einstein Condensation for the fermionic and bosonic species, respectively.

#### 5.1.1 Bose Einstein Condensation of $^{41}\text{K}$

The primary motivation of producing a BEC of  $^{41}\text{K}$  was to establish  $^{41}\text{K}$  as a coolant, enabling the production of Bose-Fermi mixtures. Potassium has another stable bosonic isotope ( $^{39}\text{K}$ ) which is more abundant (93.3%) compared with  $^{41}\text{K}$  (6.7%). The choice of  $^{41}\text{K}$  was motivated because of many drawbacks that  $^{39}\text{K}$  presents. On the one hand, the unresolved hyperfine structure in the excited electronic state limits the effectiveness of laser cooling methods and thus adversely affects the initial conditions for evaporative cooling. In addition, at zero magnetic field the triplet s-wave scattering

length is small and negative. This entails that the Ramsauer-Townsend minimum occurs at a temperature of around  $320 \mu\text{K}$  (a zero in the cross-section) [18]. This makes it additionally difficult to achieve the high elastic collision rates needed for evaporative cooling and ultimately prevents the creation of large Bose-Einstein condensates in a magnetic trap. Nevertheless, groups in Florence and Cambridge have successfully obtained a BEC of  $^{39}\text{K}$  by tuning the scattering length with Feshbach resonances and by means of sympathetic cooling with another species ( $^{87}\text{Rb}$ ) [19] [20]

In our experiment, we employ a standard method for producing a quantum degenerate gas of  $^{41}\text{K}$ . We use laser cooling, followed by evaporative cooling in a magnetic trap. Laser cooling of  $^{41}\text{K}$  is not straightforward, since the hyperfine splitting of  $4^2P_{3/2}$  between  $F'=3$  and  $F'=2$  is 14 MHz, which is the same order of magnitude as the natural linewidth of the  $D_2$  line (6.2 MHz) (Fig 5-1). The  $F=2 \rightarrow F'=3$  transition is not separated from other  $F'$  and no longer has a close transition, because off-resonant excitation to the other excited states can occur. We detune the cooling beam to the red of the whole excited state hyperfine manifold, thus increasing the capture range of the magneto-optical trap (MOT). Following [21] the same amount of laser power is used for both cooling and repumping transitions.

The slower yields  $3 \cdot 10^9$  atoms loaded in 2s into the MOT. To increase the initial atom density, a 40 ms compressed MOT phase and a 6 ms optical molasses stage follows. Figure 5.1.1 outlines the compression steps, as well as the repumper power. After the MOT and molasses stages, the atoms are loaded onto the magnetic trap and prepared in the stretched hyperfine states  $|F, m\rangle = |2, 2\rangle$  using optical pumping. This is achieved by shining  $\sigma^+$  polarized light resonant with the  $|F = 2\rangle \rightarrow |F' = 3\rangle$  transition. The quantization axis is defined by the magnetic field parallel to the incoming beam.

Evaporative cooling of  $^{41}\text{K}$  is performed in a quadrupole magnetic trap with a vertical magnetic field gradient of  $B'_z = 220\text{G/cm}$  and a horizontal gradient of  $B'_\perp = 110 \text{ G/cm}$ .

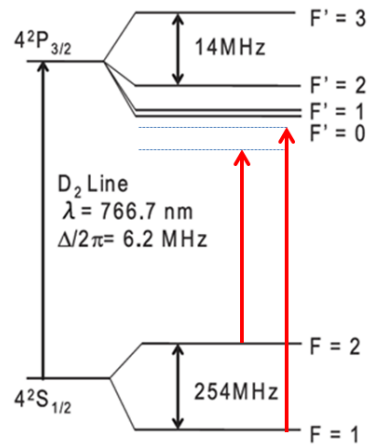


Figure 5-1: The energy level diagram of  $^{41}K$ . Hyperfine splitting between  $F'=2$  and  $F'=3$  of  $4^2P_{3/2}$  is comparable to the natural linewidth of the  $D_2$  line (6.2 MHz).

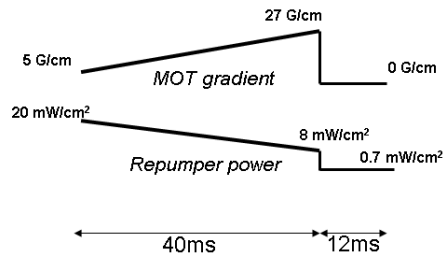


Figure 5-2: Compression steps and repumper power before loading onto the magnetic trap.

**Optical Plug** A complication in the use of quadrupole magnetic traps arises from the fact that an atom will be lost if it undergoes a transition into a non-trapped state near the magnetic field zero. This loss mechanism is referred to as a *Majorana flop*. In a classical picture, the atom is trapped as long as its magnetic moment can follow the direction of the magnetic field adiabatically, while the atom moves through the trap. As soon as the change in the magnetic field occurs too fast, the atom can flip non-adiabatically into a non-trapped state.

The magnetic moment of the atom precesses around the magnetic field. The frequency of this precession is given by the *Larmor frequency*:

$$\omega_L = \frac{|\vec{\mu}_F \cdot \vec{B}_{ext}|}{\hbar} = \frac{\mu_B |g_F m_F| |\vec{B}_{ext}|}{\hbar} \quad (5.1)$$

The atom will be confined as long as the following condition is fulfilled:

$$\omega_L \gg \left| \frac{\frac{dB_{ext}}{dt}}{B_{ext}} \right| \quad (5.2)$$

For small magnetic fields the Larmor frequency reduces to zero. Therefore, near the magnetic field zero the criterion (5.2) will not be satisfied and the atoms can escape from the trap. The region of loss is usually referred to as the *Majorana hole*. At a cold temperature in the range of microkelvins, with a gradient of 220 G/cm, the lifetime for Na, for example, is on the order of a few seconds. For our quadrupole traps, we make use of a repulsive potential of a blue-detuned laser beam. This strong dipole force repels the atoms from the hole region. The trap geometry is known as the *optically plugged quadrupole trap* and it was developed by Wolfgang Ketterle's team [3]. In our setup we use a VERDI Coherent Inc. green laser (power 15W, wavelength 532 nm) focused to a waist of 20  $\mu\text{m}$ . This creates a repulsive barrier for lithium, potassium and sodium.

The total potential is a superposition of a dipole potential  $V_{plug}$  and the magnetic potential  $V_{magn}$ .

$$V = \mu_B \sqrt{(B'/2x)^2 + (B_{y0} + B'/2y)^2 + (B'z)^2} + \frac{\alpha_K P}{\frac{\pi}{2} w^2} \exp \left( -2 \frac{y^2 + z^2}{w^2} \right) \quad (5.3)$$

Plotting this expression we obtain a faithful representation of the optically plugged potential. The gradient is 110 G/cm and the previous plug parameters have been used.

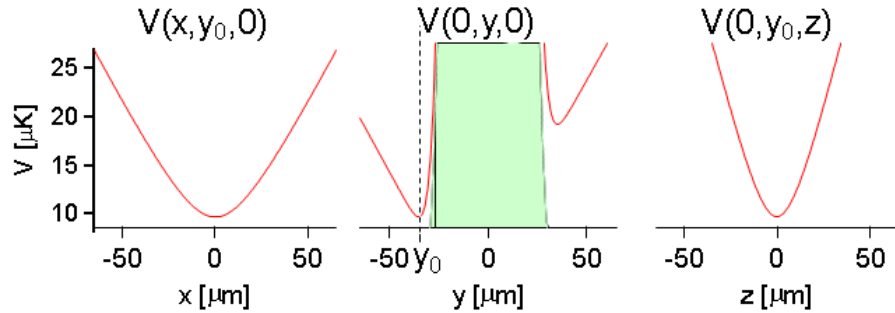


Figure 5-3: The trapping potential, essentially identical for all species, is sketched along the three axis. The plug beam is along the x-axis.  $y_0$  represents the trap minimum.

A well-centered plugged trap allows two trap minima. In order to obtain a single trap minimum  $y_0$ , in the final 2s of evaporation, a horizontal bias field is applied in the y direction, perpendicular to the plug beam.

## 5.2 Evaporation and sympathetic cooling

Evaporative cooling consists of removing high-energetic atoms from an atomic cloud, which will result in a cloud with lower temperature. These atoms carry away more than the average energy of the atom gas and therefore the temperature of the remaining atoms decreases. Evaporative cooling only works efficiently if the gas is able to thermalize and repopulate the energetic states in the Maxwell-Boltzmann distribution during the cooling procedure. As atoms are withdrawn continuously, the cloud will never reach thermal equilibrium.

In our optically plugged magnetic traps without a zero magnetic field, evaporative cooling is performed via radio frequency (RF) radiation. In the trap, atoms with higher energies can reach higher magnetic field values and therefore obtain a larger Zeeman shift. The RF frequency can be matched to the Zeeman shifted transition frequency between a trapped and a non-trapped hyperfine state. Evaporation on  $^{41}\text{K}$  is performed down to a radiofrequency of 500 kHz above the 254.0 MHz hyperfine transition of  $^{41}\text{K}$ . Below, we see the bimodal signature of a Bose-Einstein Condensate in time-of-flight absorption images. This was the first benchmark in our experiment, creation of a BEC of  $^{41}\text{K}$ .

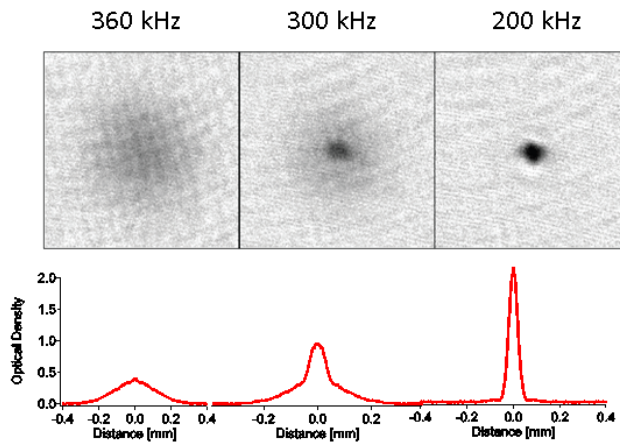


Figure 5-4: Bimodal signature of BEC by direct evaporation.

### 5.2.1 Efficiency of evaporation. Phase space density measurement for different traps

We distinguish between two regimes in the calculation of phase space density: the gradient trap regime and the harmonic trap regime. Our gradient trap is not perfectly linear, considering it is plugged with 15W of repulsive 532nm light. Hence, a harmonic approximation is appropriate to describe the bottom of the potential. These two approaches should meet at a characteristic temperature.

**PSD for bosons in a gradient trap** Let  $N$  be the total number of atoms and  $n_0$  the maximum atom density. The gradient potential is given by  $V = -\mu_B \vec{B}' \vec{r} = -\mu_B \sqrt{(B'_x)^2 + (B'_y)^2 + (B'_z)^2}$ . Hence, in thermal equilibrium the total number of atoms can be written as:

$$N = \int_0^\infty n_0 e^{-\beta V(r)} d^3 r \quad (5.4)$$

considering that  $B'_z = 2B'_x = 2B'_y = B'$ , and a change of variables from  $x \rightarrow x/2$ ,  $y \rightarrow y/2$ , we may rewrite 5.4 as:

$$N = 4 \int_0^\infty n_0 e^{-\beta B' \tilde{r}} d^3 \tilde{r} = n_0 \frac{(\beta \mu B')^3}{32\pi} \quad (5.5)$$

The phase-space density, being defined as  $\rho = n_0 \lambda_{DB}$  can be calculated for a thermal gas in a gradient trap as:

$$\rho = n_0 \lambda^3 = N \frac{(\beta \mu B')^3}{32\pi} \left( \frac{\hbar}{\sqrt{2\pi m k_B T}} \right)^3 \quad (5.6)$$

**PSD for bosons in a harmonic trap** Using the same definition as before, we need to evaluate the maximum in-trap density  $n_0$ . For a harmonic trap and considering large times ( $t \gg \omega_x, \omega_y, \omega_z$ ), the density profile is given by:

$$n_{t0f}(\mathbf{r}, t) = \frac{1}{\lambda_{dB}^3} g_{3/2}(e^{(\mu - \frac{mr^2}{2t^2})/k_B T}) = n_{3D}(0) g_{3/2}(z \exp(-r^2/R_{th}^2)) \quad (5.7)$$

The relationship between the measured  $n_{2D}$  and  $n_{3D}$  can be obtained by integrating along one dimension:

$$n_{2D} = \int_{-\infty}^{\infty} n_{3D}(\vec{r} dz) = n_{3D}(0) \sqrt{\pi} R_{th} g_2(z \exp(-r^2/R_{th}^2)) \quad (5.8)$$

rescaling distances and time we obtain the maximum in-trap density:

$$n_{3D}(0) = n_{2D}(0) \frac{g_{3/2}(z)}{g_2(z)} \frac{1}{\sqrt{\pi} R_{th}} (\bar{\omega} t)^3 \quad (5.9)$$

The deBroglie wavelength can be evaluated in the same fashion as before.

**PSD for Fermions in a harmonic trap** PSD is ill-defined as fermions approach degeneracy. In principle PSD could reach infinite values as temperature decreases. This cannot be true for fermions, since we know that they form a Fermi sea at T=0 and therefore, PSD cannot be infinity, as predicted by the  $n\lambda_{dB}^3$  expression.

Hence, instead of a thermal de Broglie wavelength  $\lambda_{dB}$ , we introduce another de-Broglie wavelength  $\lambda_v = \frac{\hbar}{m\sqrt{\langle v^2 \rangle}}$  calculated from the characteristic velocity  $v$ ; which could be the thermal velocity for thermal gases or the fermi velocity as degeneracy is approached. Let  $\sqrt{\langle v^2 \rangle} = R/t$ , where  $R = \sqrt{\frac{N}{n_{2D}}}$ . Hence, the PSD yields:

$$n\lambda_v^3 = n \frac{\hbar^3 t^3}{m^3 R^3} = \frac{n_{intrap}(\bar{\omega}t)^3 \hbar^3 t^3}{m^3 R^3} \quad (5.10)$$

$$= \frac{n_{2D}(\bar{\omega}\hbar)^3 t^6}{m^3 R^4} = \frac{n_{2D}^3 \pi^3 R_F^6 (\bar{\omega}t)^6}{6N^3} \quad (5.11)$$

This quantity can be shown to be proportional to  $T/T_F$  apart from some constant. This qualifies it as a good PSD measure, since it is 0 at T=0 and 1 when  $T = T_F$ .

### 5.2.2 PSD measurement

The necessary parameters to evaluate PSD are the following: the gradient  $B'$ , the temperature of the gas and the number of atoms. Here we describe how to obtain the three.

**B' gradient measurement** The best way to calibrate the field is to probe the atoms, and see what field (what current of the coils) exactly holds atoms against gravity. As an example, we measure that a field produced by a current of 13 A is able to hold  $^{41}\text{K}$  against gravity in our magnetic trap. By equating  $m_{k41}g = \mu B'$  we obtain  $B' = 1.1T/m$ .

Evaporative cooling of  $^{41}\text{K}$  is performed with a magnetic field gradient  $B'_z = 220\text{G/cm}$  along the vertical direction ( $B_\perp = 110\text{G/cm}$  along the horizontal direction).

For the last 2 s of evaporation the trap is decompressed to  $B'_z = 110G/cm$  to suppress three-body losses.

**Thermometry: Time-of flight measurements (TOF)** The common approach to measuring the temperature of a cloud of cold atoms is the so-called *time-of-flight* TOF imaging, where all trapping potentials are switched off and the cloud is let to expand freely until it is imaged. Absorption images are obtained by illuminating the atoms with a resonant laser beam and imaging the shadow cast by the atoms onto a CCD camera. These images integrate through one dimension to give a two-dimensional image, which we can evaluate to determine a Bose, Fermi or thermal distribution. The distribution at the wings is a 2D gaussian and its width  $\sigma = \sqrt{\langle p^2 \rangle t^2 / m^2}$  is a measure of the temperature.

$$k_B T = \frac{1}{2} m \frac{\langle \sigma \rangle^2}{t^2} \quad (5.12)$$

Thermometry measurements from absorption images of clouds can be more involved and Gaussian fits to the wings of the cloud might not be accurate enough. In addition, short TOF measurements reveal the geometry of the trapping potential and if this is asymmetric (with a certain aspect ratio), then fits to integrated 2D profiles will not give accurate results. In many cases, we have performed fits to the wings of azimuthally averaged profiles to determine the temperature. Case by case, the fitting procedure will depend on the degree of degeneracy of the gas, and whether it is a bosonic, fermionic or thermal gas.

We will refer to the reader to a thorough discussion about thermometry of Bose and Fermi gases in the Varenna notes [22] and [7].

**Measurement of atom number** To obtain the atom number from absorption images the following analysis is performed: a total of 3 pictures per cycle are taken with our ANDOR CCD camera: 1) a picture with atoms  $I_{atom}$  2) a picture with no atoms  $I_{no-atoms}$  and 3) a background picture where everything is switched off  $I_{background}$ . By subtracting the background, only the atomic cloud survives:

$$\frac{I_{atom} - I_{background}}{I_{no-atom} - I_{background}} = \frac{I_{out}}{I_{in}} \quad (5.13)$$

The atomic cloud, with a density  $n(x, y, z)$  absorbs the imaging light  $I_{in}$ . It follows from Beer's law that:  $dI/dz = -\sigma(z)n(x, y, z)I(x, y, z)$ , where  $\sigma(z)$  is the on resonance scattering cross section  $\sigma(z) = 6\pi\frac{\lambda^2}{(2\pi)^2}$

Integrating the 3D atomic density profile  $n(x, y, z)$  along the imaging direction (let us call it  $z$ ) will yield a 2D column density  $n(x, y)$ . Inserting this in Beer's equation and taking into account the magnification  $M$  and the pixel count  $A$ , we obtain the number of atoms:

$$N = -\frac{AM^2}{\sigma} \ln \frac{I_{out}}{I_{in}} \quad (5.14)$$

**Evaporation efficiency** The evaporation process should be slow to give time for elastic collisions to happen but it has to be faster than the lifetime of the atoms. The latter is mostly determined by the vacuum quality, since it is a measure of the background gas collisions that can take place. Once we had established an evaporation path towards quantum degeneracy, we measured the efficiency of the evaporation path. A good figure of merit is the quantity  $\gamma$ , defined as:

$$\gamma = \frac{-d \ln PSD}{d \ln N} \quad (5.15)$$

which measures the slope in a logarithmic plot of phase-space density PSD against atom number. An effective evaporation will lead us to an increase in PSD for every atom lost; hence a positive  $\gamma > 0$  is desired. At different stages of the evaporation process we measured the PSD by releasing the trap at predetermined times.

Because of the small fermion number ( $\approx 10^5$ ), the evaporation efficiency  $\gamma$  of  $^{41}\text{K}$  is similar with and without the fermionic load ( $\gamma \approx 3$ ). Incidentally, this is close to the result by Shin Inouye's group [21], who report an evaporation efficiency of  $\gamma = 2.7$ . The near-vertical slope in the case of fermions is a proof of efficient sympathetic cooling by  $^{41}\text{K}$ .

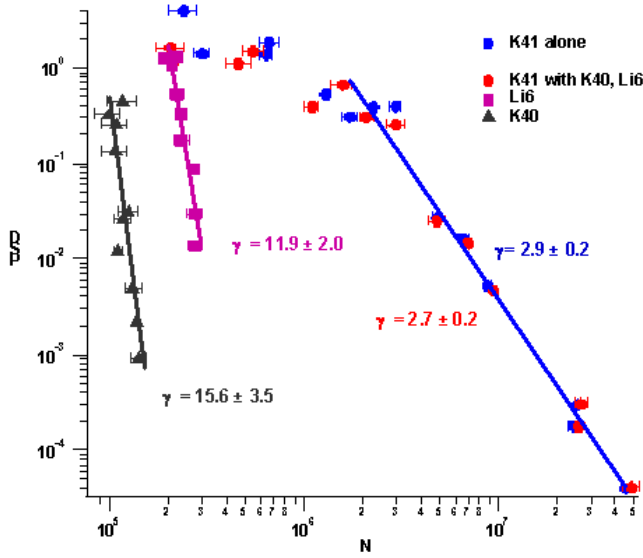


Figure 5-5: Evolution of phase-space density PSD with atom number N during evaporation of  $^{41}\text{K}$ , with and without  $^{40}\text{K}$  and  $^6\text{Li}$ . The slope  $\gamma$  indicates the evaporation efficiency.

### 5.2.3 Triply degenerate mixture of $^{41}\text{K}$ , $^{40}\text{K}$ and $^6\text{Li}$

The first important step in producing a degenerate Fermi gas of two different species is to load the mixture into a magneto-optical trap and simultaneously trap a bosonic species in to open the possibility of sympathetic cooling of the two fermionic species by the bosonic species.

Our experimental procedure consists of co-trapping  $^6\text{Li}$  and  $^{40}\text{K}$  while we load  $^{41}\text{K}$  into the MOT. We deliberately choose to load  $10^5$  fermionic atoms , since ultimately it is the bosonic coolant that will determine the maximum number of fermions that can be brought down to degeneracy. In our case,  $^{41}\text{K}$  limits the fermion number to about  $2 \cdot 10^5$ .

After loading the three species into the MOT, all three species undergo optical pumping and are prepared in the low-field seeking stretched hyperfine states of  $|F, m_F\rangle = |2, 2\rangle$  for  $^{41}\text{K}$ ,  $|F, m_F\rangle = |9/2, 9/2\rangle$  for  $^{40}\text{K}$  and  $|F, m_F\rangle = |3/2, 3/2\rangle$  for  $^6\text{Li}$ . After this state preparation, evaporative cooling of  $^{41}\text{K}$  is performed in the magnetic

trap, following the previously outlined procedure.

Optical pumping never results in a perfect state transfer, hence we developed a way to “clean up” unwanted hyperfine states. Gravity assisted state selection, consists of removing unwanted states by setting the magnetic trap to a gradient  $B'_z$  sufficient to support only stretched states such that  $\mu B'_z = mg$ . For  $^6\text{Li}$  in the stretched state  $|F, m_F\rangle = |3/2, 3/2\rangle$ , we have a total magnetic moment of  $\mu$  (1/2 from spin and 1/2 from orbital angular momentum). Hence, a magnetic field gradient of  $B'_z = 1\text{G/cm}$  will suffice to hold lithium atoms against gravity. In our case, the  $B'_z$  is reduced to 15 G/cm, thus decreasing the chances that spin-exchange collisions will occur <sup>1</sup>.

Evaporation on  $^{41}\text{K}$  is performed down to a radiofrequency of 500 kHz above the 254.0 MHz hyperfine transition of  $^{41}\text{K}$ . After evaporation, time-of-flight absorption images are taken to (destructively) probe the created mixture. We use an iXON CCD camera (ANDOR) in fast kinetic mode, whereby the camera shifts to a masked area before the next exposure is performed. The ANDOR camera is capable of shifting CCD-lines at a rate of microseconds. Using this mode, fast consecutive images of the three species can be taken before the slow electronic readout is performed. From TOF images we can extract the density profile of the 3 species and extract their temperature, atom number and relevant thermodynamic variables.

In Fig. 5-6 we see absorption images of a triply degenerate quantum gases of  $^{41}\text{K}$ ,  $^{40}\text{K}$  and  $^6\text{Li}$ , images after 8.12 ms, 4.06 ms and 1ms time-of-flight, respectively. By summing the pixels and azimuthally averaging, we obtain column densities as a function of distance measured from the center of mass of the cloud. We perform Gaussian fits to the wings (solid dots) to extract the temperature of the clouds and also Gaussian fits to the entire cloud (solid black). On top of that,  $^{41}\text{K}$  profiles were fitted with a Bose-Einstein bimodal distribution and the Fermi gases were fitted with the Fermi-Dirac distribution . We can see a sharp deviation from the Gaussian fit, which would correspond to a classical gas.

---

<sup>1</sup>Spin-exchange collisions are a cause of atom loss during evaporation. Spin exchanging collisions are inelastic. Because of the Zeeman effect, different hyperfine states have different energies, which depend on the B field. If spin-exchange happens, the energy difference between the final and initial state can be positive or negative, giving rise to exothermic or endothermic collisions. In spin-exchange collisions, the total spin  $M_{total} = m_F + m'_F$  is conserved.

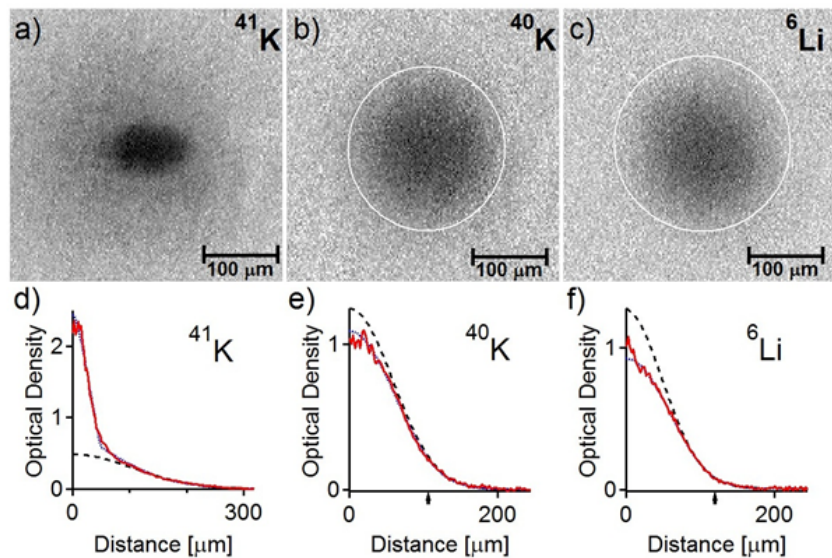


Figure 5-6: Absorption images of triply degenerate quantum gases of  $^{41}\text{K}$ ,  $^{40}\text{K}$  and  $^6\text{Li}$ , imaged after 8.12 ms, 4.06 ms and 1 ms time of flight from the magnetic trap, respectively. Atom numbers are  $1.1 \times 10^5$ ,  $2.0 \times 10^5$  and  $1.6 \times 10^5$  respectively. The white rim indicates the Fermi radius  $R_F$

To obtain relevant degeneracy parameters we need to know the Fermi temperature, which for a harmonic trap is given by:

$$k_B T_F = \hbar \bar{\omega} (6N)^{1/3} \quad (5.16)$$

$\bar{\omega}$  is the geometric mean of the trapping frequencies. We can extract this value from the trap geometry or we can use a handy formula derived for a BEC in a harmonic trap that relates the trapping frequency to critical temperature for onset of BEC  $T_C$ :

$$T_c = \hbar \bar{\omega} (N_c / \zeta(3))^{1/3} \quad (5.17)$$

where  $\zeta(x)$  is the Riemann zeta function:  $\zeta(z) = \sum_{n=1}^{\infty} n^{-z}$ . In addition, we can relate the condensate fraction  $n_c$  to the critical temperature  $T_c$ :

$$n_c = 1 - \left( \frac{T}{T_c} \right)^3 \quad (5.18)$$

We take several TOF images before and after the onset of BEC and plot condensate fraction  $n_c$  against a new variable  $x = \frac{T}{T_c}$  and fit it to the function  $n_c = \max(1 - (\bar{\omega}x^3), 0)$ . At the intercept with the  $n_c = 0$  (onset of BEC) we obtain an accurate value for the geometric mean of the trapping frequency  $\bar{\omega}$ . For  ${}^{41}\text{K}$  we obtain  $\bar{\omega} = 2\pi 380$  Hz

Expressed in Hz, we can extrapolate the trapping frequency for the fermionic species by mass scaling. Below, Fermi temperatures and Fermi radii are given for the three species:

	${}^{41}\text{K}$	${}^{40}\text{K}$	${}^6\text{Li}$
$\bar{\omega}$	$2\pi 380$ Hz	$2\pi 384$ Hz	$2\pi 993$ Hz
$T_F$	$\mu\text{K}$	$1.93\mu\text{K}$	$1.79\mu\text{K}$
$T/T_F$		0.51	0.16
$R_F$		$116\ \mu\text{m}$	$184\ \mu\text{m}$

Table 5.1: Fermi temperatures , Fermi radii and trapping frequencies for the three species, extracted from Fig. 5-6

#### **Using equilibrium thermodynamics to extract the degeneracy factor $T/T_F$ :**

The coolant brings the fermions down to degeneracy by sympathetic cooling. Assuming the three species are in thermodynamic equilibrium, once a BEC is formed, the temperature of the three gases is  $T_c$ . Under the harmonic approximation we can relate the critical temperature to the Fermi temperature of the fermions and obtain the degeneracy factor  $T/T_F$ :

$$\frac{T}{T_F} = \frac{T}{T_C} \frac{\omega_{41K}}{\bar{\omega}_{Fermion}} \frac{N_{41K}^{1/3}}{(6\zeta(3))^{1/3}} \quad (5.19)$$

If  $T = T_{C,41K}$  then,  $T = T_{F,40K} \approx 0.51$  and  $T = T_{F,6Li} \approx 0.2$ ; which is close to the values obtained before by fitting the time-of-flight distributions.

#### **5.2.4 Simultaneous observation of Pauli Pressure and Bose-Einstein Condensation**

The achievement of simultaneous Bose-Fermi degeneracy enables a direct and striking comparison between bosons and fermions at low temperatures. Moreover, in the case of the potassium isotopes  $^{41}\text{K}$  and  $^{40}\text{K}$ , the difference that gives rise to distinct quantum statistics is only one neutron. The effect of quantum statistics on the sizes and shapes of the clouds can be seen in axial and radial density profiles. For example, bosons are characterized by a shrinking profile as it gets colder and by the formation of a bimodal shaped profile with a large and narrow parabolic peak, representing the BEC. On the other hand, fermions when degeneracy is reached, form a Fermi sea and the profile does not shrink as temperature is decreased.

Inspired by the work by A. G. Truscott et al. [23] and the early BEC work [3], we set to evaluate a quantity that would show the distinct features that appear in absorption images for Fermions and Bosons. This quantity is the  $1/e$  width  $R$  of a Gaussian fitted to the fermionic or bosonic distributions. This value depends on the time-of-flight  $t$  and mass of each species, hence, a better quantity is the release energy defined as  $E = \frac{1}{2}mR^2/t^2$ . A normalized value can be obtained by dividing it with the Fermi energy  $E_F$  of each cloud (including the Bosons). This quantity is

calculated for many evaporation steps, from hot thermal clouds down to degeneracy and plotted against the normalized temperature of the clouds  $T_{^{41}K}$ . Thermometry is done by fitting Bose functions to the wings of the  $^{41}K$  distribution.

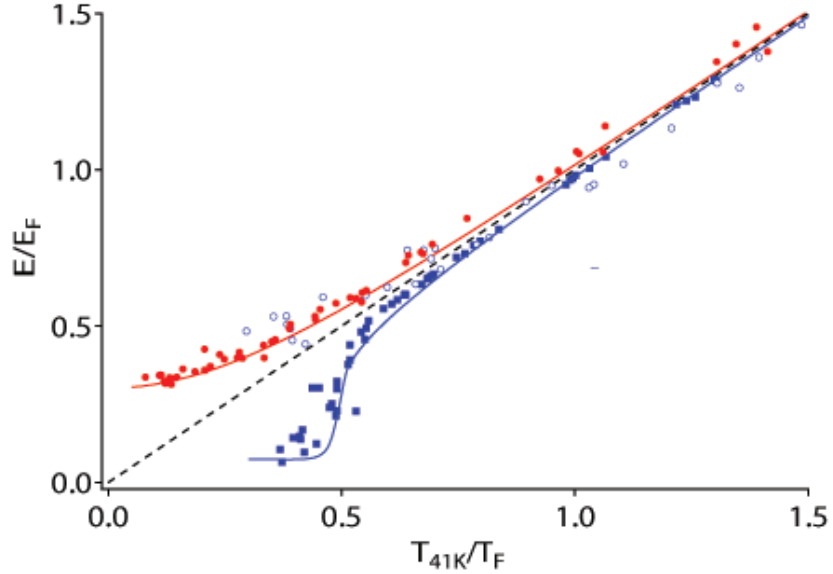


Figure 5-7: Observation of Pauli pressure and Bose condensation in a triply degenerate quantum mixture. Shown is the normalized release energy  $E/E_F$  of each cloud versus the normalized temperature  $T/T_F$ . Bose condensation of  $^{41}K$  occurs at  $T_c/T_F = 0.52$ , causing a sudden reduction in release energy below  $T_c$ . For fermions, in contrast, the release energy saturates due to Pauli pressure. Solid circles:  $^6Li$ , open circles:  $^{40}K$ , solid squares:  $^{41}K$ . Solid lines: theory for an interacting Bose gas and a non-interacting Fermi gas. Dashed line: Boltzman gas.

At high temperatures we expect  $E/k_B$  to equal the temperature of each cloud. This is why clouds collapse onto a straight line at hight temperatures. However, at low temperatures, the release energy of a trapped Fermi gas saturates, due to Pauli pressure [23]. On the other hand,  $E$  is suddenly reduced as a condensate forms. The theoretical curves shown with the experimental data were obtained by the same procedure with artificially generated clouds in a computer simulation.

## 5.3 Quantum degenerate Bose-Fermi mixture of $^{23}\text{Na}$ and $^{40}\text{K}$

Adding  $^{23}\text{Na}$  to our system opened up the possibility to study new mixtures. The initial motivation was to use sodium as a more effective coolant for both  $^{40}\text{K}$  and  $^6\text{Li}$  in order to study Fermi-Fermi mixtures. However, the Na-K mixture itself is a wonderful object of study, since it enables the creation chemically stable, fermionic ground state molecules, where strong, long-range dipolar interactions take place. In the following lines, the experimental steps leading to a Bose-Fermi mixture of  $^{23}\text{Na}$  and  $^{40}\text{K}$  are reviewed and the formed quantum mixture is analysed.

### 5.3.1 Experimental sequence

The production of a Bose-Einstein Condensate of sodium is the first step towards the formation of a Bose-Fermi mixture of Na-K. This will not be reviewed here, since most of the experimental steps are based on previous work in the CUA [13]. Addition of K gives a new twist to the experiment since it makes the mixture prone to new mechanisms of atom losses; among them, spin-changing collisions in the MOT and magnetic trap. In order to minimize losses, our group developed a method, whereby one species (Na) is loaded into the MOT, optically pumped to the stretched state  $|2, 2\rangle$  and captured in the magnetic trap, only supporting such a state against gravity. This field is left on while loading of K takes place. Hence, we say that Na has been “shelved” and this way only atoms in the stretched state are present in the optically plugged magnetic trap before K is loaded. The final atom number can be controlled by changing the MOT loading times for the two species.

After both species have been loaded into the magnetic trap, the mixture undergoes RF evaporation. Hot  $^{23}\text{Na}$  atoms in the stretched  $|2, 2\rangle$  state are removed from the trap by applying radiofrequency to couple the atoms to the untrapped state  $|1, 1\rangle$ . After decompression, a  $5\mu\text{K}$  mixture is loaded onto a crossed optical dipole trap. The lifetime of the mixture is increased by transferring the  $^{23}\text{Na}$  atoms to the hyperfine

ground state  $|1, 1\rangle$  via a Landau-Zener sweep to obtain a longer lived ( $\tau=20\text{s}$ ) mixture of  $^{23}\text{Na}$   $|1, 1\rangle + ^{40}\text{K}$   $|9/2, 9/2\rangle$ . The gas is then further evaporatively cooled by reducing the intensity of the dipole trap beams.

At the end of this scheme of evaporation, a degenerate Fermi gas of  $^{40}\text{K}$  is obtained coexisting with a Bose-Einstein condensate of  $^{23}\text{Na}$ . In Fig. 5-8 two sets of absorption images of the mixture are shown with different atom numbers.

It is important to point out the bimodal density distribution in the fermionic cloud coexisting with the large condensate. This can be explained by considering the strong attractive interaction between  $^{23}\text{Na}$  and  $^{40}\text{K}$ . As the condensate grows, we see that the fermions feel the created strong mean-field potential. This phenomenon has been studied by Ospelkaus et al. in the case of  $^{40}\text{K}^{87}\text{Rb}$ , where they measured an enhanced mean-field energy of the condensate due to mutual mean-field confinement, predicted by a Thomas-Fermi model [24].

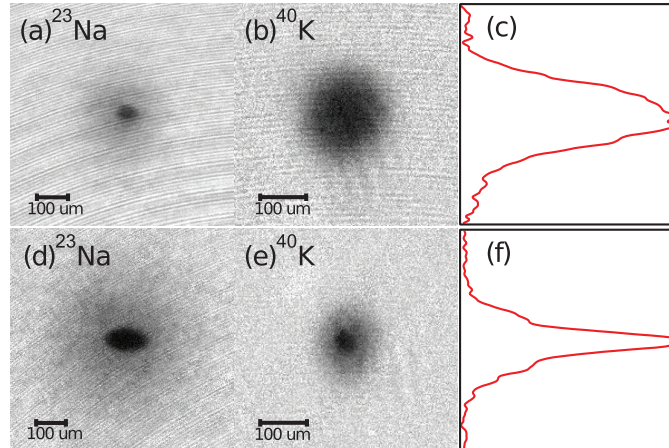


Figure 5-8: Simultaneous quantum degeneracy of  $^{23}\text{Na}$  and  $^{40}\text{K}$  atoms. Pairs of time of flight (TOF) absorption images of a  $^{23}\text{Na}$  BEC and a  $^{40}\text{K}$  Fermi cloud are shown. In e) a strong attractive interaction between the two species can be observed as a sharp increase of the central density in the fermionic cloud in the presence of a Bose condensate. c) and f) are the center-sliced column density of the fermionic clouds of b) and e) respectively. The upper row contains a 50%-50% mixture, whereas the lower row has only 8% of fermionic  $^{40}\text{K}$ . Degeneracy of fermions is  $T/T_F = 0.6$ .

### 5.3.2 Efficiency of evaporation

We studied the efficiency of  $^{23}\text{Na}$  as a coolant for  $^{40}\text{K}$  by taking absorption images of both species during evaporation. We measured the atom number and determined the temperature of the clouds by fitting a thermal profile to the wings of the bosonic species  $^{23}\text{Na}$ . Three regimes can be distinguished: 1) the magnetic trap 2) Decompressed magnetic trap and 3) ODT. Because transfers are done adiabatically, PSD is expected to be the same at the transition points.

The cooling efficiency for sodium in the magnetic trap is  $\gamma_{\text{Na}} = 2.7$ . The load on the bosons does not affect the efficiency. However, sympathetic cooling of  $^{40}\text{K}$  is not as effective, because  $^{40}\text{K}$  is seen to be lost from the trap due to three-body collisions. In the crossed-dipole trap we find that by transferring  $^{23}\text{Na}$  to  $|1, 1\rangle$ , the atoms are less confined and efficiency of evaporation of sodium is compromised  $\gamma_{\text{Na}} = 0.9$ . However, the  $^{40}\text{K}$  atom number does not change, therefore the efficiency for sympathetic cooling is high.

If we use  $^{23}\text{Na}$  only as a coolant and evaporate all of it, a degenerate Fermi gas of  $^{40}\text{K}$  is obtained at  $T/T_F = 0.35$  and  $N_{^{40}\text{K}} = 3 \cdot 10^5$ .

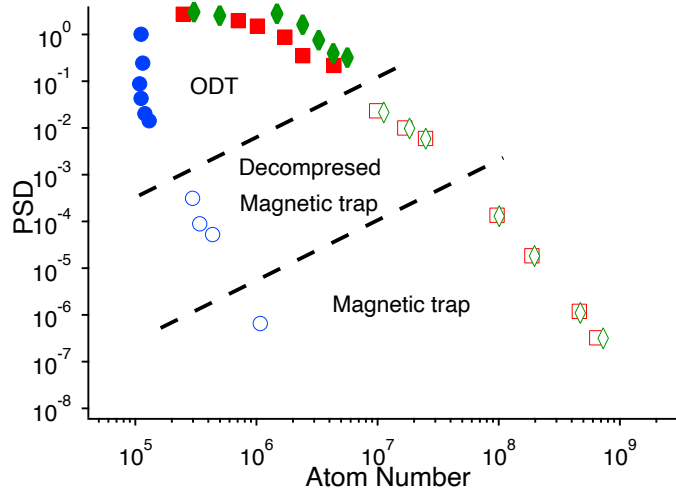


Figure 5-9: Phase-space density (PSD) evolution vs atom number N. Blue circles:  $^{40}\text{K}$ , Red squares  $^{23}\text{Na}$  with  $^{40}\text{K}$ . Green diamonds:  $^{23}\text{Na}$  alone. Empty and solid symbols represent the PSD in the magnetic trap and optical trap, respectively.



# Chapter 6

## Interactions: Feshbach resonances

Interactions are fundamental in the study of quantum gases. Although most of the physics described here occurs in dilute gases, atomic interactions determine the outcome of many cold atom experiments. In fact, no quantum degeneracy could be achieved if it not were for collisions between atoms. For example, evaporative cooling is based on the presence of elastic collisions between atoms. Beyond the mere technique, interactions form a fundamental part of the richness of ultracold science. It is through interactions that atoms are correlated and form a host of novel phases of matter, ranging from excitations in a weakly interacting Bose gas to strongly interacting superfluids or insulators.

Along with laser cooling and trapping and evaporative cooling, one of the most relevant tools in ultracold science is the ability to freely tune the interactions by use of *Feshbach resonances*[25]. By simply changing a magnetic field it is possible to tune the interaction from strongly attractive to strongly repulsive. This tool allows the experimenter to manipulate and probe interacting systems at will and test theoretical predictions as a function of interaction strength. In addition, a control over interaction can be used to produce weakly-bound molecules, also known as *physicist's molecules* or *Feshbach molecules*.

In the following, a brief introduction to the physics of interactions will be given, focusing on Feshbach resonances. The observation of many heteronuclear Feshbach resonances will also be described. These results have been published in [26] and [27].

## 6.1 Long-range and short-range interactions

The strength of an interaction between two bodies primarily depends on their distance. In the case of alkali atoms we will distinguish two clear differing regimes of interaction [28]:

On the one hand, at long-distances the electron clouds do not overlap and the main interaction is the dipole-dipole interaction between two mutually induced dipole moments. This is known as *van der Waals* interaction and it has the form of  $-C_6/r^6$ , where  $r$  is the atomic separation. The range of this potential is given by the *van der Waals length*  $l_{vdW} = \frac{1}{2} \left( \frac{mC_6}{\hbar^2} \right)^{1/4}$ , beyond which it can be neglected. In the case of Na-K, the  $C_6 = 2447 \text{a.u.}$  [29] and a range of  $l_{vdW} = 54a_0$ .

On the other hand, at short distances, electron clouds overlap and other kind of interactions start taking place. These are dominated by a strong repulsive core due to the overlapping clouds. Hence, the relative spin orientation of the outer valance electrons acquire an important role. Although at long-range their difference is negligible, the ground state potential of a singlet  $S = 0$  or triplet  $S = 1$  is very different.

In the diagram 7-4 we see an example of a *Born-Oppenheimer potential*, which will be further discussed in the next chapter. Here the ground state potential between a  $^{23}\text{Na}$  atom and a  $^{40}\text{K}$  are depicted. At short distances the singlet potential  $X^1\Sigma$  and the triplet potential  $a^3\Sigma$  are split. The reason for the singlet  $S = 0$  to have deeper minimum, relies on the fact that due to a symmetric spatial wavefunction, there will be higher overlap and hence stronger bond will be formed, as compared to atoms with opposite spins, for which the Pauli exclusion principle applies.

Because of the diluteness of our cold quantum gases ( $\sim 10^{14}\text{cm}^{-1}$ ), basically binary collisions dominate. Then the theoretical treatment is greatly simplified. We will introduce the basic two-body problem in the context of scattering theory and provide some useful notions such as, cross section, scattering length, collision channel, Feshbach resonances and other topics relevant to understanding the experimental work that has been done in the context of this thesis.

## 6.2 Ellastic and Inellastic collisions

Interactions can give rise to elastic or inelastic collisions. *Elastic collisions* do not alter the relative kinetic energy, however, they can redistribute momentum between atoms, as it happens when an ensemble is thermalized.

Inelastic collisions on the other hand, do alter the relative kinetic energy and are a primary cause of atom loss. The change in kinetic energy normally exceeds typical trap depth and atoms escape from the trap.

Let us consider the collision between two distinguishable particles. Without interactions the relative wavefunction can be written as:  $\Psi(\vec{R}) = e^{i\vec{k}\cdot\vec{R}}|1,2\rangle$ . After an elastic collision, the relative momentum is changed from  $k \rightarrow k'$  and the effects of this interaction can be described by a new wavefunction:

$$\Psi(\vec{R}) \propto \left( e^{i\vec{k}\cdot\vec{R}} + \frac{e^{i\vec{k}\cdot\vec{R}}}{R} f(E, \hat{k}, \hat{k}') \right) |1, 2\rangle \quad (6.1)$$

where  $f(E, \hat{k}, \hat{k}')$  is the *scattering amplitude* and  $|f(E, \hat{k}, \hat{k}')|^2$  describes the probability that a pair of atoms with collision energy  $E$  is scattered from relative momentum  $k$  to  $k'$  [30]. The *cross section*  $\sigma(E)$  is defined as the integral of  $|f(E, \hat{k}, \hat{k}')|^2$  over all possible momenta for a given  $E$ .

This problem is more tractable in spherical coordinates, this is why spherical harmonics are normally used. For more derivations, the reader can find a through discussion on scattering theory in a quantum mechanics textbook.

For ultracold collisions, a further simplification arises because the thermal de Broglie wavelength  $\lambda_{dB}$  is larger than the range of interaction. Considering the small density of ultracold gases, this means that the mean distance between atoms is large compared to the interaction range. Together, during collision the shape of the potential cannot be resolved by atoms. This is why the concept of *scattering length*  $a$  is crucial when dealing with cold gases; as long as two distinct potentials generate the same scattering length, then it can be shown that they describe the same many-body system. The description of the system *only* depends on the scattering length and not on the details of the interaction potential. Formally, the scattering length is defined

as the following low-energy limit:

$$\lim_{k \rightarrow 0} k \cot \delta(k) = -\frac{1}{a} \quad (6.2)$$

where  $\delta(k)$  is the s-wave phase-shift. A *positive* scattering length corresponds to a repulsive effective interaction, whereas a *negative* value indicates attractive interaction. Except close to a Feshbach resonance, the scattering cross section is energy independent and depends solely on the scattering length:  $\sigma = 4\pi a^2$

### 6.3 Feshbach resonances

It is possible to change the scattering length with an external magnetic fields. This stems from the coupling between different atomic states that share the same spin projection  $M = m_1 + m_2$  but have different total magnetic moments. The difference in energies between these states can be tuned with an external magnetic field, as the different magnetic moments will result in different Zeeman shifts. A paradigmatic example is the two channel model presented below:

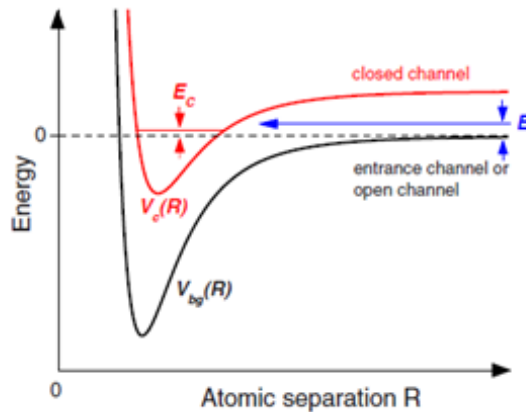


Figure 6-1: Basic two channel model for a Feshbach resonance. It occurs when two atoms colliding at energy  $E$  in the open channel resonantly couple to a molecular bound state with energy  $E_c$  supported by the closed channel. If the magnetic moments of the closed and open channels differ,  $E_c$  can be magnetically tuned. i.e. closed channel  $S=1$  (triplet) and open channel  $S=0$  (singlet)

The relative Zeeman shifts between the open and closed channels can be used to tune the energy of the last bound state into resonance with the kinetic energy of the incoming hyperfine state of the atoms. This is what is known as a *Feshbach resonance*, and the scattering amplitude is greatly enhanced by this coupling to the molecular state. As a matter of fact, the scattering length  $a$  diverges at the resonance:

$$a(B) = a_{bg} \left( 1 - \frac{\Delta}{B - B_0} \right) \quad (6.3)$$

where  $a_{bg}$  is the background scattering length, which is directly related to the energy of the last-bound vibrational state,  $\Delta$  the width of the resonance and  $B_0$  the resonance position. For  $^{23}\text{Na} |1, 1\rangle - ^{40}\text{K} |9/2, -5/2\rangle$  collisions, the scattering length has been calculated using the Asymptotic Bound State model [31],

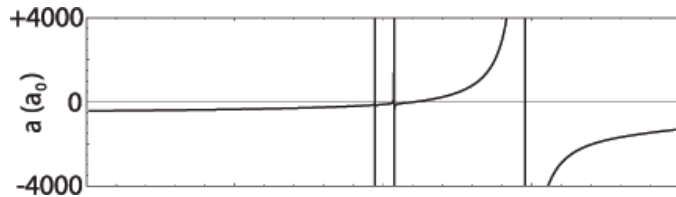


Figure 6-2: Scattering length from the ABM model as a function of B field

### 6.3.1 Feshbach spectroscopy in $^{23}\text{Na} - ^{40}\text{K}$

Once with the new degenerate Bose-Fermi mixture of  $^{23}\text{Na}$  and  $^{40}\text{K}$  at our disposal, we searched for interspecies Feshbach resonances. We performed trap loss spectroscopy using resonant losses as signatures of Feshbach resonances. These losses occur because of the release of internal energy into the motion when colliding atoms end up in a lower internal state or when a molecule is formed. The gain in kinetic energy is on the order of the Zeeman energy, the hyperfine energy, or the molecular vibrational energy, depending on the inelastic channel, and is generally so large that all atoms involved in the collisions are lost. Hence, in addition to the changes in scattering length, near a Feshbachresonance inelastic collisions are strongly enhanced [32].

Over thirty Feshbach resonances were observed in five different spin state combinations of  $^{23}\text{Na}|1,1\rangle + ^{40}\text{K}|9/2, m_F\rangle$ , from the ground spin state  $m_F = -9/2$  up to  $m_F = -3/2$  and also for  $m_F = +9/2$ . Spin states of  $^{40}\text{K}$  are prepared starting from  $m_F = +9/2$  by a single Landau-Zener sweep through the intermediate  $m_F$  states at 15 G. The observed resonance positions and widths are obtained by fitting a Gaussian to loss curves. Fig.6-3 shows the experimental loss spectra that was obtained in our experimental runs.

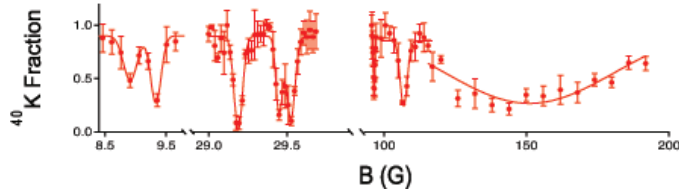


Figure 6-3: Experimental loss spectra of  $^{40}\text{K}$  in the presence of  $^{23}\text{Na}$ . Three  $s$ -wave resonances and two  $p$ -wave manifolds are found, the latter resolved in one doublet and one triplet.

The observed resonance positions for several combinations of hyperfine states in  $^{23}\text{Na}^{40}\text{K}$  and widths from phenomenological Gaussian fits to loss curves are reported in the table6.1. Many wide  $s$ -wave Feshbach resonances at low magnetic fields are identified, the widest one positioned at 148.3 G for collisions between  $^{23}\text{Na}|1,1\rangle + ^{40}\text{K}|9/2, -5/2\rangle$ , with a width of the loss feature of 37 G, see Fig. 6-3. This is an order of magnitude wider than any other resonances found so far in a Bose-Fermi mixture of chemically different atomic species.

It is known that  $p$ -wave Feshbach resonances split into a doublet structure [33]. The origin of this effect lies in the magnetic dipole-dipole interaction that induces an energy difference for the  $m_l = 0$  and  $|m_l| = 1$  quantum numbers. In the NaK systems we observed triplet features for several  $p$ -wave resonances. This structure arises from off-diagonal terms in the dipole-dipole interaction, which couple different values of  $m_l$  while conserving total angular momentum  $m_l + M_{F,K} + M_{F,Na}$ . Because of the low B field nature of the NaK  $p$ -wave resonances, we were able to resolve these structures.

We used a powerful method, developed by Tiecke et al [31], to explain the  $s$ -

Table 6.1: Observed positions of interspecies Feshbach resonances between  $^{23}\text{Na}$  in  $|1, 1\rangle$  and  $^{40}\text{K}$  atoms in  $|9/2, m_F\rangle$ . The positions and widths of the resonances,  $B_0^{\text{exp}}$  and  $\Delta B_{\text{exp}}$ , are determined by phenomenological Gaussian fits ( $\propto e^{-(B-B_0^{\text{exp}})^2/\Delta B_{\text{exp}}^2}$ ) to the observed loss features. For  $p$ -wave resonances, we report positions and widths of resolved features, i.e. doublets and multiplets.  $B_0^{\text{th}}$  and  $\Delta B_{\text{th}}$  give the theoretical positions and widths from the ABM model.

$^{23}\text{Na} 1, 1\rangle +$ $^{40}\text{K} 9/2, m_F\rangle$	$B_0^{\text{exp}}$ [G]	$\Delta B_{\text{exp}}$ [G]	$B_0^{\text{th}}$ [G]	$\Delta B_{\text{th}}$ [G]	Res. type
-9/2	6.35, 6.41, 6.47, 6.68	0.02	7.2		<i>p</i>
-9/2	19.1, 19.2, 19.3	0.02	18.3		<i>p</i>
-9/2	78.3	1.1	75.4	0.9	<i>s</i>
-9/2	88.2	4.3	86.4	7.5	<i>s</i>
-7/2	7.32, 7.54	0.2, 0.03	8.7		<i>p</i>
-7/2	23.19, 23.29	0.05, 0.05	22.1		<i>p</i>
-7/2	81.6	0.2	82.1	0.03	<i>s</i>
-7/2	89.8	1.1	87.2	0.5	<i>s</i>
-7/2	108.6	6.6	110.5	18.3	<i>s</i>
-5/2	9.23, 9.60	0.14, 0.11	11.0		<i>p</i>
-5/2	29.2, 29.45, 29.5	0.04	27.8		<i>p</i>
-5/2	96.5	0.5	97.2	0.03	<i>s</i>
-5/2	106.9	1.8	103.6	0.3	<i>s</i>
-5/2	148.3	36.5	147.7	37.4	<i>s</i>
-3/2	12.51, 12.68	0.16, 0.06	14.8		<i>p</i>
-3/2	39.39, 39.86	0.15, 0.14	37.2		<i>p</i>
-3/2	116.9	0.5	118.3	0.04	<i>s</i>
-3/2	129.5	4.6	127.0	0.24	<i>s</i>
-3/2	174.9	19.8	212.9	77.0	<i>s</i>

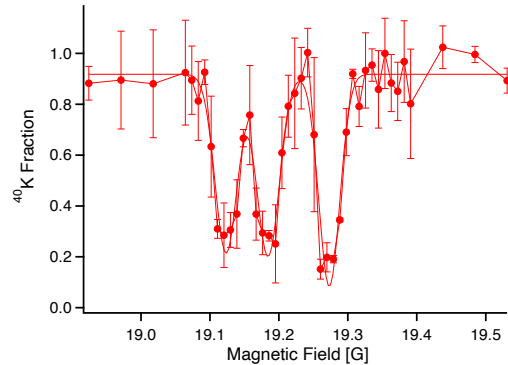


Figure 6-4: Triplet structure of the  $p$ -wave resonance at 19.1 G for the  $^{23}\text{Na}|1, 1\rangle + ^{40}\text{K}|9/2, -9/2\rangle$  spin configuration. A phenomenological triple Gaussian fit is applied as a guide to the eyes.

,  $p$ - and  $d$ -wave character of the resonance and predict their positions and widths. The main idea of the asymptotic bound state model (ABM) is that the two-body Hamiltonian:

$$H = H_{rel} + H_{int} = \frac{\mathbf{p}^2}{2m_r} + V + H_{hf,Na} + H_{hf,K} \quad (6.4)$$

is diagonalized and the energy of the bound molecular states is varied to fit known resonances. The input parameters are the singlet and the triplet scattering length  $a_s$  and  $a_t$  and the  $C_6$  coefficient to describe the van der Waals tail of the interatomic potential. A big computational advantage is that it is not necessary to solve the radial Schrödinger equation.

The model is called asymptotic because it is assumed that the detailed behaviour of the potential at small interatomic distances can be neglected as the main contribution to the position of Feshbach resonances stems from the asymptotic behaviour of the atoms. With only three input parameters a first calculation of the position of Feshbach resonances can be done (similar to the multichannel quantum defect model [34]).

The theoretical values obtained with this model are shown in Table 6.1. The ABM approach leads to a refined triplet bound state energy of  $E_t^s = -1654(3)$  MHz and  $E_t^p = -1478(7)$  MHz, and using the long range potential from Ref. [35], we find a new value of the triplet scattering length of  $a_t = -830(70) a_0$ . The Feshbach resonances we find are ten times broader than in KRb [36] and lie at low fields, making NaK a remarkable system for Bose-Fermi mixtures.

### 6.3.2 Feshbach spectroscopy in $^{41}\text{K}$ - $^{40}\text{K}$ and $^6\text{Li}$ - $^{41}\text{K}$

We also observed interspecies Feshbach resonances between  $^{41}\text{K}$  -  $^{40}\text{K}$  and  $^6\text{Li}$ - $^{41}\text{K}$ . These are listed in the table below. Some of the theoretical predictions and s and p wave assignments were done using a coupled-channel calculation by Andrea Simoni (LENS, Florence).

A wide Feshbach resonance is found in collisions of  $^{40}\text{K}$  in state  $|9/2, 9/2\rangle$  with  $^{41}\text{K}$  in state  $|1, 1\rangle$  at 543 G. This resonance opens the door to study an isotopic Bose-

Mixture	$B_0$ [G]	$\Delta B_{\text{exp}}$ [G]	Resonance type
$^6\text{Li}   1/2, 1/2\rangle   ^{41}\text{K}   1, 1\rangle$	31.9	0.2	s-wave
$^6\text{Li}   1/2, 1/2\rangle   ^{41}\text{K}   1, 1\rangle$	335.8	1.1	s-wave
$^{40}\text{K}   9/2, 9/2\rangle   ^{41}\text{K}   1, 1\rangle$	472.6	0.2	s-wave
$^{40}\text{K}   9/2, 9/2\rangle   ^{41}\text{K}   1, 1\rangle$	432.9	2.5	p-wave
$^{40}\text{K}   9/2, 9/2\rangle   ^{41}\text{K}   1, 1\rangle$	542.7	12	s-wave

Table 6.2: Observed interspecies Feshbach resonances between  $^6\text{Li}$ - $^{41}\text{K}$  and  $^{40}\text{K}$ - $^{41}\text{K}$  atoms. The width of the resonance,  $\Delta B_{\text{exp}}$ , is determined by a phenomenological gaussian fit to the observed loss feature (see e.g. Fig. 6-3). For the  $p$ -wave resonance, the width was measured at  $T = 8 \mu\text{K}$ .

Fermi mixture ( $^{40}\text{K}$ - $^{41}\text{K}$ ) with essentially no gravitational sag and wide tunability. This tunability is very exciting, as the classic example of isotopic mixtures,  $^3\text{He}$ - $^4\text{He}$ , did not allow to access a large region of the complex phase diagram of Bose-Fermi mixtures. It could certainly become a clean model system for strongly interacting Bose-Fermi mixtures.



# Chapter 7

## NaK, testbed for ultracold molecular physics

### 7.1 Molecules: Building blocks of nature

Everything surrounding us, including ourselves, is made of molecules. In nature we find 80 different elements that correspond to stable atoms, but these atoms can form larger entities, which we call molecules. The physical, chemical and biological properties of matter depend on how these 80 stable atoms come together and interact giving rise to the most relevant natural processes.

A molecule is a specific discrete grouping of atoms in a definite geometrical arrangement [28]. They can be as simple as the diatomic molecules that will be discussed in this thesis:  $H_2$ ,  $NaK$ ,  $H_2O$  or more elaborate ones, like DNA, composed of many thousands of atoms. Almost all molecules, be they organic or inorganic, consist of atoms of no more than half a dozen of elements. This is one of the wonders of nature, that so much diversity can be obtained from few building blocks; in the same way two dozen letters are enough to produce the world's literature.

It is the quest of molecular physics and chemistry to determine the laws that hold atoms together in a molecule, what spatial structure they form and how stable it is, what the binding energy of atoms in the molecule is and ultimately, understand how these properties translate into function. An illustrative example of how a single atom

can entirely change the properties of a molecule can be found in *cyanidin*, which is the pigment that makes cornflowers (*Centaurea cyanus*) blue and poppy red [37]. While being the same molecule, it only differs by one hydrogen atom, due to the different acidity in the sap of the flowers: *cyanidin* loses a hydrogen in an alkali environment like cornflowers, whereas it acquires one if the sap is acidic (hydrogen rich), like in poppy.

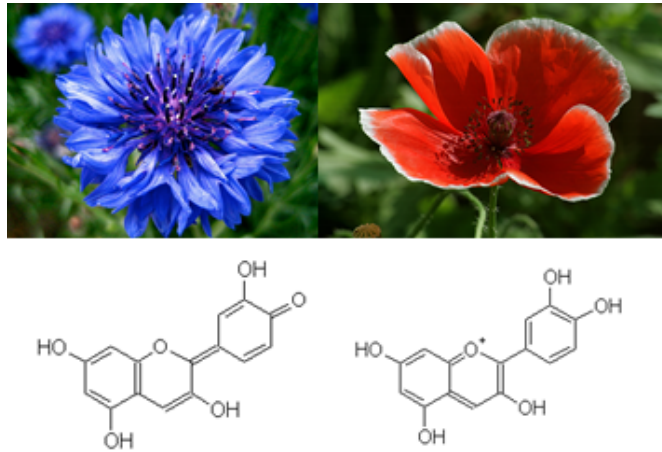


Figure 7-1: In the cornflower (left) the sap is alkaline, and the cyanidin molecule loses a hydrogen ion and turns blue. In the poppy (right) the sap is acid; because the molecule is in an environment rich in hydrogen ions, it acquires one and turns red.

With this example, we see that different molecules give rise to different colors. It follows that the molecular structure has something to do with the energy transitions associated with absorption of light. Indeed, an extra hydrogen  $H^+$  makes electrons more localized in the molecule, hence more energetic light will be absorbed (blue light) and the flower will acquire the complementary color red. On the other hand, by removing an extra  $H^+$  electrons will be less confined and the light it absorbs will be redder, hence the blue color of basic cornflower.<sup>1</sup>

---

<sup>1</sup>As a simplified model, the "electron in a box" provides the intuition that a confined electron in a smaller space tends to make energy level spacings larger. A back-of-the-envelope calculation readily tells us that the energy spacing for a particle confined to a distance  $a$  is inversely proportional to  $a$  and given by  $\Delta E = \frac{\hbar^2}{8ma} \Delta n$ . A covalent bond is roughly 150pm long (e.g. diamond) and absorbs in the ultraviolet, hence they are colorless. However, electrons that can spread over many atoms within

Molecules, like the ones that give color and energy to flowers, were long considered an abstraction, but are now taken for granted in any natural science. Before delving into the study of cold molecules it is of interest to briefly address how this came about, almost at the same time when atomic theories were being developed.

### 7.1.1 The Molecular Hypothesis

The concept of molecule (Lat. *molecula*), which means "small mass", although used in vague terms by Descartes, was first introduced in the scientific debate as a result of two discoveries in the 19th century. The first was John Dalton's *law of Definite and Multiple Proportions*, precursor of what we understand today as stoichiometry, namely, that the ratio of the masses of elements that mix together are fixed whole numbers. The second powerful idea that pointed towards the existence of molecules was formulated in 1811 by Amedeo Avogadro when interpreting Gay-Lussac's measurements on gas mixtures in the framework of Dalton's atomism, he stated his hypothesis, also known as the the *Molecular hypothesis*: "For a given volume, and under the same pressure and temperature conditions, all gases have the same number of molecules". This is the familiar ideal gas law <sup>2</sup>; however, its relevance lies in the clear distinction he made between atoms and molecules. A quote from his 1849 article [38] reveals an almost modern description of molecules:

*It seems to me that one can think of the combination of several atoms of different kinds only as their union into a single molecule, in which one can no longer distinguish the parts of the volume that belong to the individual atoms. The atmospheres of imponderable bodies<sup>3</sup> that surround the atoms in the separated state, and that hold them at a certain distance from one another, and thus determine the volume, should interpenetrate and become combined, in such a way as to form only a single atmosphere for the entire molecule, surrounding the individual atoms, and bringing*

---

a molecule will absorb in the visible, if they are confined to between 600pm and 800pm according to this simple model

<sup>2</sup>Avogadro's law is stated mathematically as:  $\frac{p_1 \cdot V_1}{T_1 \cdot n_1} = \frac{p_2 \cdot V_2}{T_2 \cdot n_2} = const.$

<sup>3</sup>replacing "imponderable bodies" by "electron cloud" would be the current picture of a molecule

*them rather closer together than are the resultant molecules themselves,  
and thus determining the molecular volume of compounds.*

The recognition by Avogadro of the distinction between atoms and molecules was a key step in the development of modern chemistry, since it allowed for the first time to give correct formulas to compounds and understand reactions of gaseous elements. Avogadro deduced correctly that the elementary particles in gases such as chlorine and hydrogen are not atoms but diatomic molecules,  $Cl_2$  and  $H_2$ , and the reaction is therefore  $H_2 + Cl_2 \rightarrow 2HCl$ . James Clerk Maxwell in 1879 published in Nature an article under the title *Molecules*, in which he gave the current definition of a molecule:

*An atom is a body which cannot be cut in two; a molecule is the smallest possible portion of a particular substance.*

It took many decades until a formal demonstration of the existence of molecules was given by Jean Baptiste Perrin in 1908. Careful experiments and quantitative analysis of *visible* phenomena like Brownian motion, allowed Perrin to convince the scientific community of what he called *la réalité moleculaire*. Most notably, the existence of molecules was proved indirectly by measuring Avogadro's constant <sup>4</sup>  $N_A$  in different experimental settings and showing that they all coincided. The success of the *Molecular hypothesis* together with the on-going quantum revolution paved the way to a new theory of the chemical bond, coherent with quantum mechanics, masterfully developed by Pauling, Heitler, London and others.

Perrin made use of an *ultramicroscope*, a tool that allowed him to observe suspended jittering particles of a smaller size than the wavelength of light. He did this by shining a convergent beam at right angles with the microscope objective. Precursor of modern single-molecule techniques, this kind of light scattering experiments allowed scientists to observe molecular agitation for the first time. It was not until 2009 that a research group in IBM was able to obtain a first close-up image of a single

---

<sup>4</sup>The number of molecules in 1 *mole* is called Avogadro's constant  $N_A = 6.022 \cdot 10^{23}$ . If a volume of a gas of 22.4 litres at 1 atm pressure and at a temperature of 0°C contains only one kind of molecules; then its mass is equal to the molecular mass multiplied by 1 g. e.g. 32 g for a gas of  $O_2$  and 2 g for a gas of  $H_2$ . This is a mole and it contains  $N_A$  molecules.

molecule using an atomic force microscope. Such an experimental feat, that probed the electron cloud of a molecule (pentacene), made the atomic backbone of a single molecule directly visible for the first time.

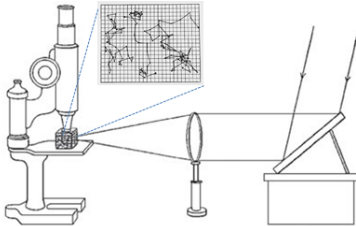


Figure 7-2: Brownian motion measurement by Perrin. Illuminating colloidal particles from the side scatters light, making them visible[39].

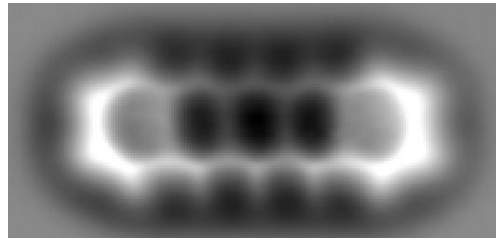


Figure 7-3: Inner structure of a pentacene molecule imaged with an atomic force microscope

From Perrin's ultramicroscope to AFM measurements, a multitude of experimental methods have contributed in the journey to understand molecular structure. These include, X-ray diffraction, mass spectrometry, NMR etc. Current technology makes it also possible to calculate the structure and the binding energies of small and medium sized molecules by *ab initio* methods using fast computers. Undoubtedly, experimental input is essential for a successful determination of molecular structures and this is where optical spectroscopy has played a major role. By making use of light-matter interactions, spectroscopists have probed the inner structure, geometry, energy levels and properties of molecules with high accuracy for many decades. As will be described in subsequent sections, these tools are now being used not only to probe, but also to manipulate molecules and bring them to desired quantum states.

### 7.1.2 Molecular spectroscopy: probing molecules

The investigation of molecular structure by spectroscopic techniques parallels the study of atomic structure, in that the methods of quantum mechanics are applied along with the information obtained from molecular spectra. By producing a sample of a given molecule and studying its absorption or emission of light, the energies and relative intensities of transitions can be identified.

If a molecule absorbs or emits a photon of energy  $h\nu$ , it makes a transition from a state with energy  $E_1$  to another state of energy  $E_2$ . Conservation of energy dictates that:

$$h\nu = E_1 - E_2 \quad (7.1)$$

These states can be discrete, and therefore they will correspond to a sharp peak in the spectrum representing a bound state. Coupling to continuum states will broaden the spectra, as it happens with transitions from or into dissociations states of the molecule.

Atomic energy states are essentially determined by different configurations of the electron cloud. Molecules, on the other hand, have more internal degrees of freedom, such as the relative motion of nuclei and their geometric arrangement. This makes molecular spectra much more complicated but also more interesting!

A lot of information can be extracted from spectra: The line intensities are a measure of the transition probabilities and their measurement can be used to test calculated wavefunctions of the states between which the transitions occur. From the linewidth, the lifetimes of the involved states can be determined and finally, the splitting of the lines in external fields gives information on the electric and magnetic moments of the molecule. In the following, spectroscopic notation will be used and transition frequencies will be given in wavenumber units<sup>5</sup>  $\tilde{\nu} = 1/\lambda$ .

Interactions between constituent atoms are not strong enough to constrain them completely, if this were so, molecules would behave in the same way as atoms<sup>6</sup>. To

---

<sup>5</sup>Even though they are not SI unit, wavenumbers are still widely used in the field of spectroscopy and it is convenient in atomic and molecular physics, as they provide a measure of both wavelengths and energy levels. Usually given in the unit of  $\text{cm}^{-1}$ , the wavenumber  $\tilde{\nu}$  describes how many wavelengths fit into the length of one centimeter  $\tilde{\nu} = 1/\lambda$ . It has the advantage that this is proportional to the photon energy  $E = h\nu$ , so that energy differences can be added and subtracted easily, as the energy required to drive a transition will be given by the difference in wavenumbers. As frequency is the other useful unit in atomic physics, the conversion below will come in handy:

$$\nu = c\tilde{\nu} \rightarrow 1\text{cm}^{-1} \hat{=} 29.978\text{GHz} \quad (7.2)$$

$$\tilde{\nu} = \frac{\nu}{c} \rightarrow 1\text{GHz} \hat{=} 0.03336\text{cm}^{-1} \quad (7.3)$$

<sup>6</sup>Nuclear energies are of the order of 10 MeV, atomic energies of the order of 10 eV (UV); however, chemical interactions, such as covalent bond, are smaller, corresponding to  $\approx 5\text{eV}$ .

	Electronic	Vibration	Rotation
$E(cm^{-1})$	40000	1500	10
$E(eV)$	5	0.2	0.001
$\lambda(\mu m)$	0.3	6	1000
T(K)	60000	2000	10

Table 7.1: Energy scales in a diatomic molecule

list the main differences: first of all, molecules posses more electronic states than atoms. The nuclei in the molecule can *vibrate* around their equilibrium points and in addition, the whole molecule can *rotate* around axes through its center of mass.

Therefore, for each electronic molecular state, there are many vibrational and rotational energy levels (sometimes called *ro-vibrational*). Measured molecular spectra can be classified as follows:

- Transitions between rotational levels for the same vibrational and electronic state lead to rotational spectra in the microwave region ( $\lambda \approx 1mm$  to  $1m$ )
- Transitions between rotational levels in different vibrational levels of the same electronic state, lead to vibration-rotation spectra in the mid-infrared wavelengths ( $\lambda \approx 2.5 - 25\mu m$ )
- Transitions between two different electronic states have wavelength from the UV to the near infrared ( $\lambda \approx 100nm-2\mu m$ . )

### 7.1.3 Experimental methods in Molecular Physics

At first spectroscopists studied spectra that took the form of arrays of lines and dense bands on photographic films. But by improving gratings and eventually using tunable lasers, bands could be resolved into lines. In recent years, a number of experimental techniques for the investigation of molecules have been developed and improved [40]. This includes Fourier spectroscopy, synchrotron radiation spectroscopy, electron spin resonance spectroscopy, mass spectrometry, molecular beam techniques etc. These techniques can be classified into three different categories: spectroscopic techniques,

scattering experiments (study of collisions), macroscopic experiments (diffusion, viscosity in molecular gases ).

To this list, it is necessary to add the recent developments in ultracold science, that have allowed the cooling of molecules. Laser cooling and trapping, magnetic trapping and evaporative cooling, creation of degenerate ultracold quantum gases and the discovery of hosts of Feshbach resonances have led to a revolution in experimental physics, ultimately leading to the formation of ultracold molecules in their lowest possible quantum state, where rotational and vibrational motions are absent. The experimental approach will be described in subsequent chapters, once a clear picture of modern spectroscopic tools has been discussed.

NaK is one of the heteronuclear alkali diatomic molecules which has been most frequently studied spectroscopically. The preferred method that has been used to map out the molecular potentials of alkali molecules has been Fourier-transform spectroscopy. A detailed presentation of this technique can be found in [28]. The experiment is normally done in a heat pipe, although with the advent of cold atoms techniques, higher accuracy can be obtained in MOTs. The development of a useful heatpipe is not straightforward, since homonuclear molecules also form and most of the times the alkalis at hand have very different melting temperatures. By adding argon buffer, molecule formation is localized and prevents windows from coating. Heat pipes have been refined to be amenable to spectroscopy of diatomic molecules; one such example is the concentric heatpipe [41] in which alkali A and alkali B are at different temperatures, thus providing the ability to control their partial pressures.

Fourier Transform spectroscopy overcomes the limitations encountered when scanning frequencies individually over a narrow range of wavelengths at a time; as it would happen using a grating as a dispersive element. Instead, in Fourier transform spectroscopy, a broadband light source is used and sent into the beamsplitter of a Michelson interferometer. One of the beam hits a fixed mirror and the other one a moving mirror, whose position is recorded with an infrared laser. Then the beam is directed into an absorption cell or a MOT and as output an *interferogram* is produced, i.e. a function of intensity vs. time. This is converted into an absorption or

emission spectrum by means of a Fourier transform, which can be readily computed with a computer program, once a digitized signal is created.

Most of the groups who have reported on molecular potentials of NaK have made use of a similar setup to excite NaK molecules and measure fluorescence signals. Russier-Antoine et al. have evaluated extensively the electronic ground state  $X^1\Sigma^+$  of NaK. Tiemann et al. have improved these measurements and calculation by observing more spectral lines of the triplet state.

This spectroscopic technique enables the recording of broad spectra, exhibiting 100 MHz resolution with an accuracy of  $10^{-9}$  in wavenumber and  $10^{-2}$  in intensity. The performance of Fourier transform spectrometers may be drastically boosted by using frequency-combs as an excitation source. Our group has implemented a Ti:Saph CW ring laser for high resolution spectroscopy of NaK energy levels.

## 7.2 Understanding molecular potentials

When we think of molecules, simple mechanistic models of their structure come to mind, in which we picture atoms in space with well-defined geometric shape and symmetry. Nuclei are glued by the averaged spatial distribution of electrons (what Avogadro called “atmospheres of imponderable bodies”) bonding the nuclei together against repulsive forces of positive charges. This picture, which is static, corresponds to the *equilibrium structure* of the nuclei, and it is a minimum of the total energy of the molecule. To avoid any complications that arise when considering moving reference frames, we will assume the molecule to be at rest in the laboratory frame.

We will make use of quantum mechanics for a quantitative discussion on molecular interactions. A free molecule at rest consisting of  $k$  nuclei and  $n$  electrons in a state with total energy  $E$  is described by the Schrödinger equation:

$$\hat{H}\Psi = \left( -\frac{\hbar^2}{2m} \sum_{i=1}^n \nabla_i^2 - \frac{\hbar^2}{2M_k} \sum_{k=1}^k \nabla_k^2 + V(r_1, \dots, r_k, R_1, \dots, R_k) \right) \Psi = E\Psi(r_1, \dots, r_k, R_1, \dots, R_k) \quad (7.4)$$

Even for the simplest molecule we can think of ( $H^+$ ), this equation cannot be solved exactly. One can try to solve it numerically, but the accuracy will depend on the method, computational capability and specifics of each problem. A more physical approach is to make sensible approximations, leading to a simplified and solvable Schrödinger equation. In this spirit, we introduce the fundamental approximation of molecular physics: the *adiabatic approximation* or Born-Oppenheimer approximation.

### 7.2.1 The Born-Oppenheimer approximation

The first step in reducing the complexity of the task is permitted by the separation of energy scales. The motion of the electrons in a molecule is fast enough to neglect the motion of the molecule (electron dynamics is of the order of 100s of THz, whereas vibrational motion of nuclei is of the order of THz). This approximation, also known as the *frozen nucleus approximation* is good for cold atoms and molecules, however, it breaks down when dealing with light atoms (for which isotopic shifts need to be taken into account). For heavy atoms with mass number of  $A$ , the isotopic difference in energy scales as  $\frac{1}{A^2}$  and thus can be negligible. Here we give an introduction to the Born-Oppenheimer approximation, the original derivation can be found in [42].

We write the total Hamiltonian as

$$H = H_e^{BO} + T_n + \sum_i \vec{l}_i \cdot \vec{s}_i + H_{HFS} \quad (7.5)$$

where the  $H_e^{BO}$  is the electronic part,  $T_n$  the kinetic part for the nuclear motion and  $\sum_i \vec{l}_i \cdot \vec{s}_i$ , the spin-orbit and  $H_{HFS}$  hyperfine parts.  $T_n$  has the form:

$$T_n = \frac{p_n^2}{2\mu} + \frac{\vec{l}^2}{2\mu r^2} \quad (7.6)$$

The eigenvalues of  $H_e^{BO}$  give the electronic energies as a function of internuclear separation  $r$ , which are then taken as potentials  $U(r)$  for the Hamiltonian in the

subspace of the nuclear motion:

$$H_n = T_n + U(r) \quad (7.7)$$

It is with these adiabatic potentials that we will deal with in the rest of the discussion. By applying the BO approximation, we are assuming that the nuclear motion is infinitely slow compared to the electrons. As done in every separation of variables problem, here too, the total wavefunction will be a product form of electronic and nuclear wavefunctions

$$\Psi(r_i, R_i) = \chi(r_i)_{electrons} \Psi(R_i)_{nuclei} \quad (7.8)$$

and the total energy will result in the sum of the electronic energy  $E_e$ , vibration  $E_v$  and rotation  $E_J$ .

The simple form of the total energy allows one to draw energy schemes like those for atoms, but the terms become potential functions with vibrational and rotational energy levels. One can describe a great part of molecular physics with these potential energy diagrams. An example of a calculated potential energy curve for NaK as a function of interatomic distance is given below. Labelling of states is done in the following way: the ground state is labelled as  $X$ . States that have the same spin multiplicity<sup>7</sup> as the ground state are labelled in alphabetical order with capital letters from the energetically lowest state (except  $X$ ) to higher states. Following the Roman letter, a Greek letter will indicate the projection of the orbital angular momentum along the internuclear axis. Following the convention for atomic angular momentum states,  $\Sigma$ ,  $\Pi$  and  $\Delta$  correspond to  $L = 0$ ,  $L = 1$  and  $L = 2$ , respectively. The spin multiplicity is indicated as a superscript and another letter g for *gerade* (symmetric) or u for *ungerade* (anti-symmetric) is added after the Greek letter to indicate the reflection symmetry along an arbitrary plane containing the internuclear axis in the case of homonuclear molecules.

---

<sup>7</sup>2S+1 where S is the total spin quantum number of the molecule. ie.e, S=0, singlet, S=1 triplet etc,

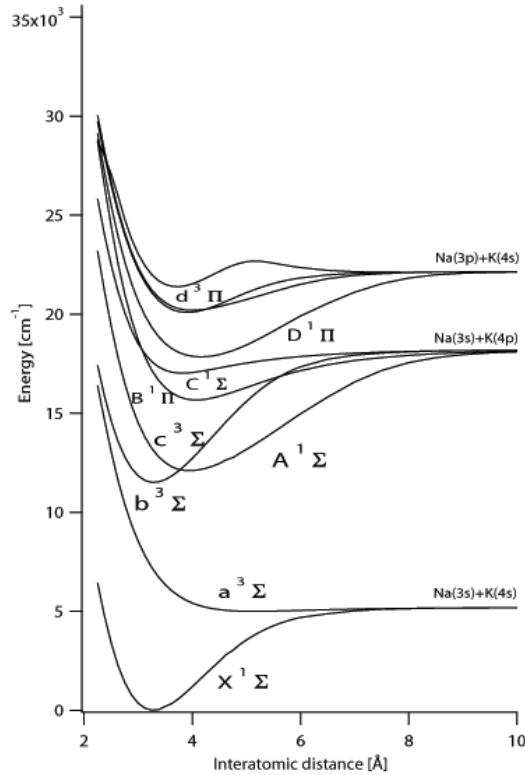


Figure 7-4: Potential energy curve of NaK. Spectroscopic constant extracted from ab initio calculation[43]

### 7.2.2 Model potentials

We cannot directly measure the potential energy, the observables are only the energy level differences of bound states in the potentials. With modern computational tools, numerical solutions can be obtained to Schrödinger's equation, and in an iterative fashion fit accurate molecular potentials to experimentally measured energies. Such an example is given in Figure 7-4 . However, it is very useful to consider model potentials, the easiest one being the harmonic oscillator, centered at the equilibrium internuclear separation  $r_e$ . The minimum potential energy and the stiffness of the oscillator are chosen in such a way that the lowest eigenvalues accurately match empirical data. The next step in correctly describing the potential is by introducing

anharmonicities; with these, higher energy levels will match with the model and will discard the possibility of infinite bound vibrational levels, something unphysical and therefore inappropriate if we are to draw conclusions about weakly-bound ultracold molecules.

An ideal model needs to satisfy the following requirements:

- as  $R \rightarrow \infty$ , the asymptotic value should equal to the total energy of two free atoms in a configuration that connects to a molecular state.
- the potential should become infinite as  $R \rightarrow 0$ , because of the repulsion between nuclei at small distances.
- the potential should have a minimum,

The simplest satisfactory option is the Morse potential, which is described by:

$$U(R) = D_e[1 - \exp -a(R - R_e)]^2 \quad (7.9)$$

where  $D_e$  represents the depth of the potential minimum <sup>8</sup>. The Morse potential has analytic solutions and gives accurate predictions for the first low-lying levels. When looking up spectroscopic data, we will encounter values of the corresponding Morse coefficient, as well more elaborate expansion coefficients. In the case of NaK, [43] these are the listed values for the ground state:

	$R_e$ ( $\text{\AA}$ )	$\omega_e$ ( $\text{cm}^{-1}$ )	$D_e$ ( $\text{cm}^{-1}$ )
(1) $\Sigma^+$	3.49	124.01	5275

Fig.7.2.2 shows a comparison between the Morse potential and more accurate model potential.

As mentioned, anharmonicities and asymptotic behaviour can be widely improved by adding more parameters. One way to express experimentally obtained  $\nu$ th energy levels is via the Dunham expansion.  $\nu$ th vibrational and rotational energy levels,

---

<sup>8</sup>Some authors correctly make the distinction between the  $D_e$ , potential depth, and  $D_0$ , the dissociation energy required to break apart the lowest vibrational level. They are not the same and careful attention should be paid when using data from the literature.

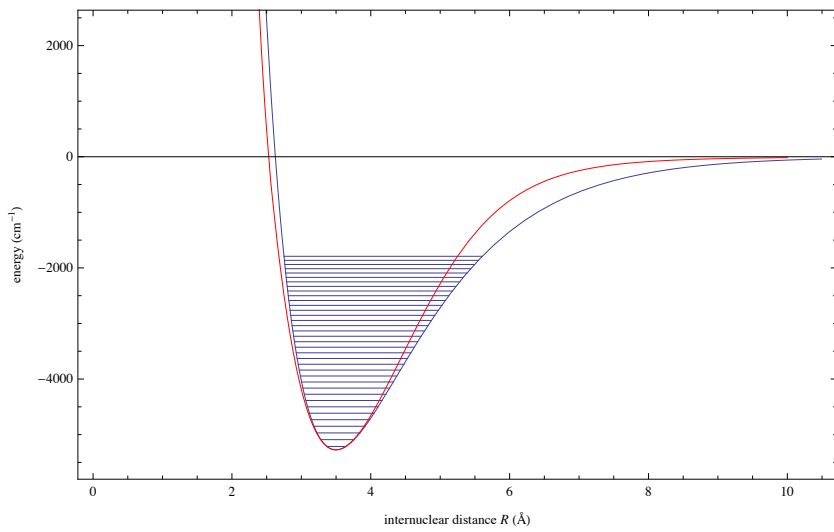


Figure 7-5: Morse potential energy curve of NaK from ab initio calculation [43] (blue) and accurate potential from Tiemann [29] (red). Levels are eigenvalues of the Morse potential up to  $\nu = 35$ .

$G(\nu)$  and  $B(\nu)$ , respectively, can be expressed in terms of the Dunham coefficients  $Y_{il}$  as:

$$G(\nu) = \sum_{l=1} Y_{l,0} (\nu + 1/2)^l = \omega_e (\nu + 1/2) - \omega_e \chi_e (\nu + 1/2)^2 + \dots \quad (7.10)$$

$$B(\nu) = \sum_{l=1} Y_{l,1} (\nu + 1/2)^l = B_e - \alpha_e \omega_e (\nu + 1/2) + \gamma_e (\nu + 1/2)^2 + \dots \quad (7.11)$$

For the singlet and triplet ground state of NaK, the most up to date coefficients are given in [29] and [44]. Gerdès et al. [44] have improved the triplet ground state potential and provide the current state of the art ground state potential for NaK.

Many model potentials have been developed that include these corrections and Dunham expansions, the most widely used one being the Rydberg-Klein-Rees method (RKR). This method appears in the literature as a standard procedure to reproduce spectroscopic measurements of the chemical bound region. Its basic features will be discussed here.

There exists a large collection of computer codes for the numerical solution of converting the measured differences in energy levels as a function of the vibrational quantum number  $\nu$  and rotational quantum number  $J$ ; i.e.  $E(\nu, J)$  to the desired potential function  $U(r)$ . Under the Born-Oppenheimer approximation, the starting point for integration is the classical action integral which we will use for the long-range interaction analysis of the LeRoy-Bernstein approach 7.24.

$$\nu + \frac{1}{2} = \frac{2\mu}{\pi\hbar} \int_{R_1(\nu)}^{R_2(\nu)} \sqrt{E(\nu) - V(r)} dr \quad (7.12)$$

Based on this first order semiclassical approximation and assuming  $\nu$  to be continuous, two key equations from the vibrational energy levels  $G(v)$  and rotational constants  $B(v)$  are derived. For a given eigenvalue  $E_0$ :

$$f = \frac{\hbar}{(2\mu)^{1/2}} \int_{-1/2}^{\nu_0} \frac{d\nu}{(E_0 - E(\nu, J))^{1/2}} = \frac{1}{2}(R_{max} - R_{min}) \quad (7.13)$$

$$g = \frac{(2\mu)^{1/2}}{\hbar} \int_{-1/2}^{\nu_0} \frac{hB(\nu)d\nu}{(E_0 - E(\nu, J))^{1/2}} = \frac{1}{2}\left(\frac{1}{R_{max}} - \frac{1}{R_{min}}\right) \quad (7.14)$$

where  $f$  and  $g$  are related to the classical turning points  $R_{max}$  and  $R_{min}$  for a given state at energy  $E_0$  as:

$$R_{min}(\nu) = \sqrt{f^2 + f/g} - f \quad (7.15)$$

$$R_{max}(\nu) = \sqrt{f^2 + f/g} + f \quad (7.16)$$

Repeating this procedure for all observed vibrational levels yields a potential energy function against interatomic distance. Normally a table of turning points on selected energy levels is given. For checking the validity of these potentials, one recalculates the eigenstates by the radial Schrödinger equation using this potential point wise and interpolating, for example, by cubic splines.

Many molecular physicists try to give an analytic function as a best representation of the potential (see [29]), while others give a point wise RKR table. There is no general consensus as to what approach is the best. Ultimately, both ways need to accurately reproduce the observed spectra. Calculated potentials are a necessary starting point that will guide experiments in cold collisions and cold molecules.

### 7.2.3 Angular momentum in molecules and Hund's cases

Given these potentials, what are the good quantum numbers? Depending on the energy scale, many kinds of angular momenta are coupled with each other in molecules. A list of angular momenta is given here: electronic orbital angular momentum, rotational angular momentum, electronic spin and nuclear spin. The complexity of molecular spectra is largely due to the coupling between these angular momenta.

Hund's classification is a way to understand which coupling is relevant in what case. In this discussion, Hund's case (a) and (c) will be elaborated, since they are the most important for cold molecule experiments.

Hund's case (a) is the most ubiquitous case when dealing with deeply bound molecules. Electronic interaction  $H_e$  contributes primarily to the hamiltonian, while the spin-orbit term and the rotational energy are small perturbations. Hyperfine interaction is also neglected in this case, because it is much smaller than other angular momenta. If we are dealing with a deeply bound molecule, such as NaK in its lowest vibrational state, then it corresponds to Hund's case (a). In this case, state labelling follows the previously mentioned notation for orbital angular momentum  $\Lambda$ .

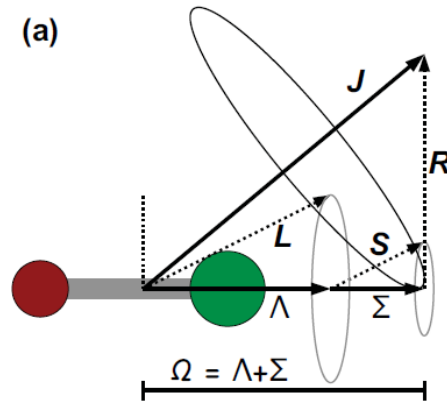


Figure 7-6: Hund's case(a), free precession of  $L$  and  $S$  around the internuclear axis, due to small spin-orbit coupling.

Hund's case (c) is a rare case in nature but very relevant in cold atom experiments, since it corresponds to loose, fluffy molecules in the asymptotic limit. Here the energy of spin-orbit interaction dominates over that of electronic interaction and hyperfine interactions. Rotation is neglected because near dissociation the size of the molecule is large, corresponding to small rotational energy. The labelling of these states is done by projecting the sum of orbital angular momentum and electronic spin onto the molecular axis. This projection is named  $\Omega$ . Hunds coupling case c) is valid for internuclear distances approximately larger than  $20a_0$ , where  $a_0$  is the Bohr radius,

beyond which the interaction is governed by the Van der Waals force.

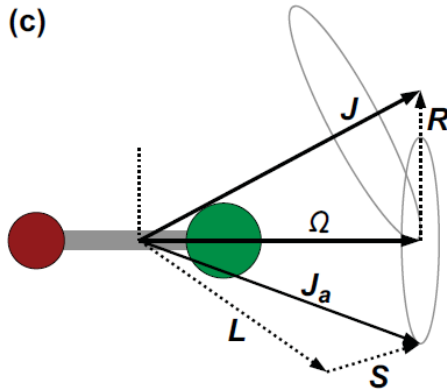


Figure 7-7: Hund's case(c), strong spin-orbit coupling with  $\vec{L} + \vec{S} + \vec{R} = \vec{J}_a$  and  $J$  precessing around the internuclear axis.  $R$  is the rotational angular momentum, which is normally neglected for ultracold molecules.

#### 7.2.4 Molecule-Light interactions: Molecular transitions and selection rules

In the same way as with atoms, light manipulation of molecules requires some knowledge of how light interacts with molecules. In this section, the most relevant aspects of optical transitions in molecules will be given, focusing on electric dipole transitions, since other transitions such as electric quadrupole or magnetic dipole transitions are smaller.

First, let us list the selection rules for various cases. As a rule of thumb, the total angular momentum  $J$  should satisfy:

$$\Delta J = 0, \pm 1 \quad (7.17)$$

with the exception of  $J = 0 \rightarrow J' = 0$ . In addition, the symmetry of the molecule restricts transitions between  $+ \rightarrow +$  and  $- \rightarrow -$ , only allowing transition between  $+$  and  $-$ .  $\pm$  refers to the symmetry of the wavefunction under spatial inversion

(change/unchange). For homonuclear molecules this notation is changed to g (gerade) and u (ungerade) and only transition between g and u are allowed.

Apart from these rules, we need to consider how angular momenta are coupled, as discussed in the previous section. In Hund case (a), the quantum number  $\Lambda$  should satisfy:

$$\Delta\Lambda = 0, \pm 1 \quad (7.18)$$

which means that transitions like  $\Sigma \rightarrow \Sigma$  and  $\Sigma \rightarrow \Pi$  are allowed but transitions like  $\Sigma \rightarrow \Delta$  are not. An additional selection rule comes from the spin component:

$$\Delta S = 0 \quad (7.19)$$

which indicates that singlet-singlet and triplet-triplet transitions are allowed but singlet-triplet transitions are forbidden. This is a relevant point when considering a transfer of molecules to the lowest vibrational state.

For Hund's case (c), i.e. in the long-range limit, the restrictions apply to the angular momentum  $\Omega$  as,

$$\Delta\Omega = 0, \pm 1 \quad (7.20)$$

These rules do not hold exactly in a real molecule, especially when considering mixed states in which singlet and triplet states are mixed. An extended discussion on selection rules and molecular transitions can be found in [28].

### 7.2.5 The Franck-Condon Principle

So far the selection rules apply to the angular components of the molecular wavefunction, in a similar way as when dealing with atoms. In molecules, however, the nuclear wavefunctions also need to be considered. In a classical model, which gives intuitive insight into electronic transitions, the absorption or emission of a photon occurs within a time interval that is short compared to the vibrational period of the molecule. The transition is so fast, that the size of the molecule does not change when the transition happens. In a quantum mechanical language, this selection rule can be

interpreted by requiring a significant overlap between ground and excited wavefunctions for a transition to occur. This is readily confirmed by considering the matrix element of the corresponding transition. The insensitivity of nuclei to the optical frequencies responsible for electronic transitions lets the matrix element separate as follows:

$$\langle \Psi_g \chi_g | \vec{d} \cdot \vec{E} | \Psi_e \chi_e \rangle = \langle \Psi_g | \vec{d} \cdot \vec{E} | \Psi_e \rangle \langle \chi_g | \chi_e \rangle = \hbar \Omega_R \langle \Phi(\nu') || \Phi(\nu) \rangle S(J', J) \quad (7.21)$$

where electronic, vibrational and rotational wavefunctions have been separated in accordance with the Born-Oppenheimer approximation.  $\Omega_R$  is the Rabi frequency and  $S$  is the Hönl-London factor (rotational strength factor) and will not be a relevant factor for ultracold molecule production, because we will be dealing with s-wave molecules in their ground state. The overlap of the initial and final nuclear wavefunctions  $\langle \Phi(\nu') || \Phi(\nu) \rangle$  provides a factor which multiplies the atomic matrix element, which is called *Franck-Condon factor*. The factor is close to 1 (when normalized) for strong molecular transitions, but it can be negligible for transitions between very different vibrational states. For a given electronic state, the Franck-Condon factors will sum to 1 for all possible vibrational transitions.

The Franck-Condon factor can be calculated numerically starting with the known molecular potentials. A straightforward technique makes use of turning points to locate states of high overlap. The turning point method shown in the diagram works because most of the amplitude of the wavefunction occurs at the turning point, where the kinetic energy is small and the wavefunction large. Hence, two states with classical turning points at similar internuclear distance  $R$  will have a large Franck-Condon factor; in contrast, two states with very different turning points will not have high overlap of their wavefunctions and consequently the Franck-Condon Factor will be small.

In a potential diagram the electronic transitions between the two states can then be represented by vertical arrows. This means, that the internuclear distance  $R$  is

the same for the starting point and the final point of the transition. Below, we see a transition from the ground state of NaK to the excited state  $B^1\Pi$ . The strongest overlap occurs between  $\nu = 0$  and  $\nu' = 2$ .

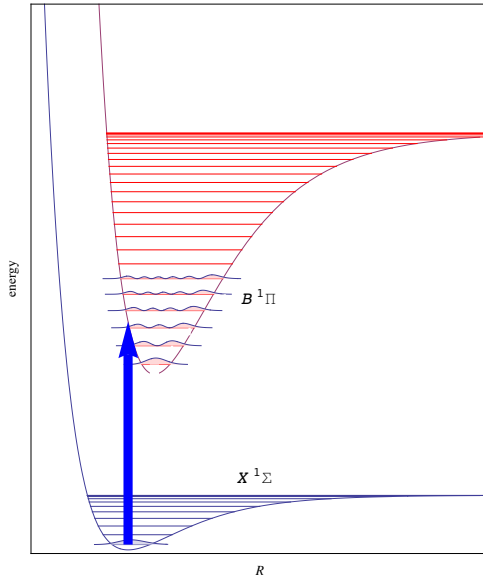


Figure 7-8: NaK potentials from [44]. The largest amplitude of the ground state wavefunction overlaps with the state indicated by the straight arrow. Units are arbitrary.

### 7.2.6 Long-range interaction: asymptotic potential

The most important part of the potential for determining the behavior of weakly-bound molecules is at long-range. For large separations, the interatomic interaction is mostly due to the Van der Waals force between two atoms. We can express the long-range potential as:

$$V(R) = D_e - C_n/R^n \quad (7.22)$$

where  $D_e$  is the dissociation energy and  $n$  can take values  $n=3$  and  $n=6$ , depending on the atomic states.

Let us consider an energy range  $\Delta$  below the atomic asymptote, (i.e. the limit where the molecule dissociates) in an interval which is small compared to the potential depth  $D_e$ :  $\Delta \ll D_e$ . If we take one bound state close to dissociation and the next higher one, both corresponding wave functions will only differ in the long range by one additional node. However, the oscillatory behaviour in the inner part of the potential is almost indistinguishable. Thus, the vibrational spacing of the levels close to the asymptote is mostly determined by the long range component of the potential. This idea is at the core of both approaches that are presented here: the analytic calculation for the asymptotic level structure by LeRoy and Bernstein [45] and the accumulated phase method by Verhaar [46].

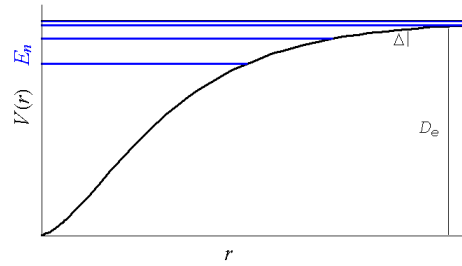


Figure 7-9: Long range potential

## LeRoy-Bernstein Approximation

LeRoy and Bernstein developed an analytic expression for transitions close to the dissociation limit. Here we will derive this relation and use it to make predictions about the long-range behaviour of NaK.

Following LeRoy's approach [45], the Van der Waals potential  $V(r) = D - \frac{C_n}{R^n}$  in the first order WKB semiclassical approximation is considered. The energy  $E(\nu)$  of the vibrational state  $\nu$  is implicitly given by the quantization condition for the phase integral  $\Phi(E)$

$$\Phi(E(\nu)) = \frac{1}{\hbar} \int_{r_1}^{r_2} p(r) dr = \left( \nu + \frac{1}{2} \right) \pi$$

Here  $p(r)$  is the local momentum and  $k(r)$  is the local wavevector

$$p(r) = \sqrt{2\mu(E(\nu) - V(r))} = \hbar k(r) \quad (7.23)$$

The inner and outer turning points of the classical motion are labelled  $r_1$  and  $r_2$ :  $V(r_1) = V(r_2) = E(\nu)$ . Following LeRoy and Bernstein,

$$\nu + \frac{1}{2} = \frac{2\mu}{\pi\hbar} \int_{R_1(\nu)}^{R_2(\nu)} \sqrt{E(\nu) - V(r)} dr \quad (7.24)$$

Although the allowed eigenvalues correspond to integer  $\nu$ , it will be treated as a continuous variable. Differentiation with respect to  $E$  leads to:

$$\frac{d\nu}{dE(\nu)} = \frac{\sqrt{\mu}}{\pi\hbar\sqrt{2}} \int_{R_1(\nu)}^{R_2(\nu)} \frac{1}{\sqrt{E(\nu) - V(r)}} dr \quad (7.25)$$

we introduce the following change of variables:  $y \equiv R_2(\nu)/R$ . From the turning

points equality we know that  $E(\nu) - D = -\frac{C_n}{R_2^n}$ . Hence,

$$\frac{d\nu}{dE(\nu)} = \frac{\sqrt{\mu}}{\pi\hbar\sqrt{2}} \int_1^{R_2/R_1} \frac{y^{-2}(-R_2^n/C_n)^{1/2}}{\sqrt{-1+R_2^n/R_1^n}} dy \quad (7.26)$$

$$= \frac{\sqrt{\mu}}{\pi\hbar\sqrt{2}} \frac{C_n^{1/n}}{[D-E(\nu)]^{1/2+1/n}} \int_1^{R_2/R_1} \frac{dy}{y^2\sqrt{y^n-1}} \quad (7.27)$$

In the limit of  $R_1(\nu) \rightarrow 0$  the integral equals  $\int_1^\infty y^{-2}(y^n-1)^{-1/2}dy = \sqrt{\pi} \frac{\Gamma(1/n+1)}{\Gamma(1/2+1/n)} \frac{n}{C_n^{1/n}}$ .

This gives an analytic expression for :

$$\frac{dE(\nu)}{d\nu} = \hbar \left( \frac{2\pi}{\mu} \right)^{1/2} \frac{\Gamma(1+1/n)}{\Gamma(1/2+1/n)} \frac{n}{C_n^{1/n}} [D - E(\nu)]^{(n+2)/2n} \quad (7.28)$$

$$= K_n [D - E(\nu)]^{(n+2)/2n} \quad (7.29)$$

Hence, an integration yields the well-known LeRoy-Bernstein formula, where  $\nu_D$  is a constant whose integer part measures the number of levels in the potential and  $H_n \equiv \binom{n-2}{2n} K_n$ .

$$E(\nu) = D - [(\nu_D - \nu)H_n]^{\frac{2n}{n-2}} \quad (7.30)$$

This equation describes the vibrational ladder by a simple power law in  $(\nu_D - \nu)$ , which for the van der Waals interaction has an exponent of 3 ( $n = 6$ ). One can extend this formula to include potential corrections such as rotational energy contributions. If the hyperfine structure is to be included in the potential, such an analytic result is not valid. The hyperfine interaction becomes important for near-dissociation states. In the low vibrational states (like in Hund's case (a)), the hyperfine interaction can be neglected. The LeRoy-Bernstein formula given here can be valuable as a first order approximation interpretation of observed spectra. We can use it for  $^{23}\text{Na}-^{40}\text{K}$  for which  $C_6 = 2447(\text{a.u.})$  [47]. The binding energy  $D - E(\nu)$  will have an upper bound value of  $E_b^* = H_{n=6}^3$

$$E_b^* = \left( \hbar \left( \frac{2\pi}{\mu} \right)^{1/2} \frac{\Gamma(1+1/6)}{\Gamma(1/2+1/6)} \frac{n}{C_6^{1/6}} \right)^3 = -1264\text{MHz} \quad (7.31)$$

### Analytic Improvement of the LeRoy Bernstein approximation

A further improvement of this formula considers the short-range part of  $V(r)$ . Usually this is a complicated expression and it is helpful to use the previous quantization rule and obtain the scattering length as a function of the energy  $E_n$  of a near-threshold bound state. Following Gribakin and Flambaum [48], we can write the scattering length  $a$ , as a sum of the mean scattering length  $\bar{a}$ , which only depends on the potential tail and a further term which is a function of the whole potential via  $\Phi(E(v))$ .

$$a = \bar{a} + \frac{b}{\tan(\pi\Phi(E))} \quad (7.32)$$

both the threshold length  $b$  and  $\bar{a}$  depend on the potential tail, and hence on the  $C_6$  coefficient. We introduce the scaling factor  $\beta_6 = \left(\frac{2\mu C_6}{\hbar^2}\right)^{1/4}$ . Then,

$$b = \frac{\beta_6}{\sqrt{2}} \frac{\Gamma(3/4)}{\Gamma(5/4)} \quad (7.33)$$

$$\bar{a} = \frac{1}{\sqrt{2}} \left( \frac{\sqrt{2\mu C_6}}{4\hbar} \right)^{1/2} \frac{\Gamma(3/4)}{\Gamma(5/4)} \quad (7.34)$$

A detailed calculation of the integrals for  $r^{-\gamma}$  potentials gives an analytic expression for  $\Phi(E)$  [49], where the coefficients represent integrals that have been evaluated for  $\gamma = 6$  (see 7.2.6)

$$\Phi(E) = \frac{2bk - (dk)^2}{2\pi[1 + (Bk)^4]} + \frac{(Bk)^4}{1 + (Bk)^4} \left( \frac{-1}{8} + \frac{D}{2\pi(k\beta_6)^{2/3}} + \frac{\Gamma(2/3)(k\beta_6)^{2/3}}{4\sqrt{\pi}\Gamma(7/6)} \right) \quad (7.35)$$

Table 7.2: Parameters characterizing the potential tail. Integrals have been calculated for  $\gamma = 6$  [49].

Coefficient	$\gamma=6$
$b/\beta_6$	0.4779888
$\bar{a}/\beta_6$	0.4779888
$d/\beta_6$	0.4579521
$B/\beta_6$	0.93323
$D/\beta_6$	0.4089698

### 7.2.7 Example with NaK from known s-wave scattering length and $C_6$

From the definition of the scattering length, we can solve for  $\Phi(E(k)) \bmod \pi$ . On the other hand, from [7.35 ]  $\Phi E(k)$  the energy can be solved for unambiguously, if only real solutions are considered.

For  $^{23}\text{Na}^{40}\text{K}$  it is known that,  $a_{singlet} = 69_{-2}^{+1}a_0$  ,  $a_{triplet} = -830(70)a_0$  and  $C_6 = 0.1179302 \cdot 10^8 \text{cm}^{-1} \text{\AA}^6$ , solving for  $\Phi$  yields:

$$\Phi_s(E) = (0.39 \pm 0.01)\text{rad} \quad \Phi_t(E) = (0.9741 \pm 0.01)\text{rad} \quad (7.36)$$

and the weakest bound state energy is calculated to be:

$$E_{singlet} = (-158 \pm 10)\text{MHz}; \quad E_{triplet} = (-1682 \pm 60)\text{MHz} \quad (7.37)$$

This approach can be performed backwards, i.e. the experimental measurement of the binding energies leads to a refinement of the values for  $C_6$  and scattering lengths. Ultimately by performing this calculation iteratively, a more accurate molecular potential will be obtained.

### 7.2.8 Accumulated Phase method

The radial Schrödinger equation for the relative radial motion of the atoms can be integrated numerically. Normally, knowledge of the inner part of the potential can be incorporated if the scattering length is well known. The phase shift is simply related to the scattering length  $a$  defined by

$$a = \lim_{k \rightarrow 0} \left[ -\frac{1}{k} \tan \delta_0(k) \right] \quad (7.38)$$

where,

$$E = \frac{\hbar^2 K^2}{2\mu} \quad (7.39)$$

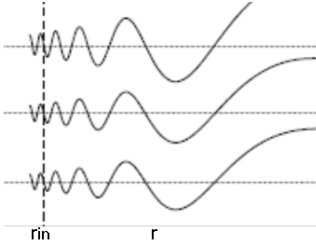


Figure 7-10: The behavior of the wavefunction phase near the inner turning point for three different energies.

Starting from  $r = \infty$ , one has to solve the equation:

$$\left( \frac{\hbar^2}{2\mu} \frac{d^2}{dr^2} - V(r) + E \right) f(r) = 0 \quad (7.40)$$

where  $f(r) \propto \sin k(r - a)$  for  $r \rightarrow \infty$ . Using this boundary condition, the wave function at any distance can be readily obtained by inward integration. As we can disregard the inner part of the wave function, the integration is stopped before the actual potential  $V(r)$  diverges from its asymptotic form, having obtained the positions of the outermost nodes. We set the inner turning point to be  $r_{in} = 18a_o$ <sup>9</sup>, which satisfies the conditions set in [46]. Let us first reduce (7.40) to a general form, where lengths have been divided by the scaling factor:  $\beta_6 = \left(\frac{2\mu C_6}{\hbar^2}\right)^{1/4}$

$$\left( \frac{d^2}{dx^2} + \frac{1}{x^6} - \tilde{k}^2 \right) y(x) = 0 \quad (7.41)$$

let us note that the wavenumber and scattering length have been scaled as well,  $\tilde{k} = k\alpha$  and  $\tilde{a} = a/\alpha$ ,

For the threshold wave function ( $k = 0$ ), the boundary conditions can be approx-

---

<sup>9</sup>Other values around  $(18 \pm 1)a_0$  yield similar results.

imated to:

$$y(x) = -1 + x/\tilde{a} \quad (7.42)$$

$$y'(x) = 1/\tilde{a} \quad (7.43)$$

Using these boundary conditions as starting point at  $x = \infty$ , the radial Schrödinger equation is integrated inwards. Then, switching the energy to a negative eigenvalue, integration is performed outwards again, while looking for the eigenvalues that satisfy the correct boundary condition at large  $r$   $y(r \rightarrow \infty) = 0$ . Numerical integration yields the following result:  $E_s = (-148 \pm 25)$  MHz and  $E_t = (-1619 \pm 50)$  MHz.

Using the same approach, p-wave binding energies can be calculated as a function of the s-wave energies by integrating the Schrödinger equation inwards, while adding the centrifugal barrier to the potential. Only the region around the p-wave centrifugal barrier changes the accumulated phase, the inner part of the potentials remain the same for s- and p-wave potentials, so this region does not contribute to the shift between energies. This method has been used to determine the free parameters for Feshbach resonance assignment in the context of the Asymptotic Bound State Model (ABM).

## 7.3 Towards ultracold ground state molecules of NaK

### 7.3.1 Production of molecules via Feshbach resonance

To make a quantum gas of polar molecules of NaK in their absolute ground state, a two step process needs to be done. In the first step, weakly bound Feshbach molecules need to be produced. In the vicinity of the resonance position at  $B_0$ , where the two channels are strongly coupled, the scattering length  $a$  is very large. For large positive  $a$ , a “dressed molecular state exists with a binding energy given by:

$$E_b = \frac{\hbar^2}{2m_r a^2} \quad (7.44)$$

where  $m_r$  is the reduced mass of the atom pair. In this limit,  $E_b$  depends quadratically on the magnetic detuning  $BB_0$ . Molecules formed in this regime are extremely weakly bound, and they are described by a wavefunction that extends far out of the classically allowed range. These considerations show how a Feshbach resonance is inherently connected with a weakly bound molecular state. A Feshbach molecule is a highly excited molecule, existing near the dissociation threshold and having an extremely small binding energy as compared to the one of the vibrational ground state. Therefore, it is not a *conventional* molecule and our traditional picture of molecular covalent bonding has to be changed. The experimental realization of Feshbach molecules is commonly done by a magnetic field ramp across the resonance. More details on alternative ways of realizing Feshbach molecules can be found in the review by Chin et al. [25].

### 7.3.2 STIRAP scheme

Molecules created via Feshbach resonances can be transferred to many other states near threshold or to much more deeply bound states. Following the techniques developed at JILA. Using a STIRAP transfer, two coherent pulses can transfer the

Feshbach molecule to the rovibrational ground state by coupling to an intermediate excited state. Accurate calculations can be done with what we know about NaK to obtain an excitation scheme with high Franck-Condon coefficients, that will guarantee an efficient molecular transfer. Below an estimate of the frequency ranges we need are given. The chosen excited state is appropriate because it mixes singlet and triplet states, hence highly excited feshbach molecules with triplet character can be transferred to the lowest vibrational singlet.

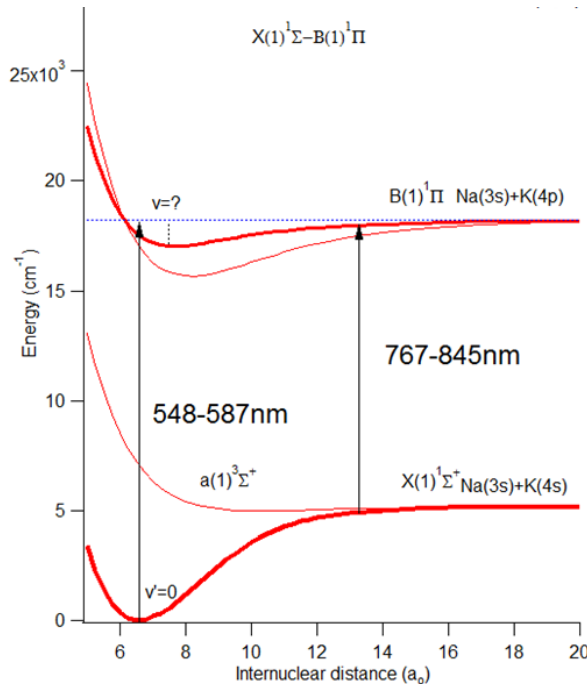


Figure 7-11: Excitation scheme for formation of NaK ground state molecules.

### 7.3.3 Reactivity of NaK in the ground state

Reactivity of molecules is a relevant property that can be advantageous in some cases, when studying ultracold chemistry of molecules. Reactivity of molecules, expressed as molecule loss from a trap, is a signature of two-body interactions and depends strongly on applied external electric fields as demonstrated with KRb in [50]. On the

other hand, nonreactive molecules have the advantage of being chemically stable in their absolute ground state, thus helping reach long-lived polar molecules.

If both atomic species are in their absolute ground state, inelastic two-body collisions are impossible, but there remains the possibility of *reactive collisions*, where a more deeply-bound state is formed, while giving energy to a third partner. Unlike other alkali dimers, such as KRb, collisional stability is guaranteed for NaK because atom exchange and trimer formation reactions are endothermic. The energy exchange  $\Delta E$  of the atom exchange reaction  $\text{NaK} + \text{NaK} \rightarrow \text{Na}_2 + \text{K}_2$  can be calculated from available data on the dissociation energy  $D_e$ .

	$D_e(\text{cm}^{-1})$	Ref
$\text{Na}_2 (\Sigma^+)$	6022.0420(40)	[51]
$\text{K}_2 (\Sigma^+)$	4450.906(50)	[52]
$\text{NaK} (\Sigma^+)$	5273.62(10))	
$\Delta E$	+74.3(3) endothermic	

It may therefore be concluded that the NaK dimer is stable with respect to atom exchange collisions in the ground rovibrational state. A more general result shows that this is true for other heteronuclear alkali dimers commonly used in ultracold atom experiments, with the exception of Li dimers and KRb, which have exothermic atom exchange reactions.[53][54]. The table below shows the energy changes and their sign (+ endothermic) and (- exothermic) for some of these alkalies.

Table 7.3: Energy change  $\Delta E_2$  for the reactions  $2\text{XY} \rightarrow X_2 + Y_2$  (in  $\text{cm}^{-1}$ ). Combinations in bold are energetically forbidden

	Na	K	Rb	Cs
Li	-328(2)	-533.9(3)	-618(200)	-415.38(2)
Na		<b>+74.3(3)</b>	<b>+45.5(5)</b>	<b>+236.75(2)</b>
K			-8.7(9)	<b>+37.81(13)</b>
Rb				<b>+291(1.5)</b>

On the other hand, for trimers such as  $\text{Na}_2\text{K}$  or  $\text{NaK}_2$  there are no empirical values

of their atomization energy <sup>10</sup>. However we can take a range of different geometric configurations for these molecules and calculate their energy using a computer simulation. This was done in [53] and the table below summarizes the atomization energies for the equilibrium structure of these molecules. The empirical dimer dissociation energies need not be simulated, as they have been measured in many spectroscopy experiments. The estimated error in the computer simulation that is reported is 5% [53].

	Atomization energy ( $cm^{-1}$ )	Reaction	$\Delta E$
Na <sub>2</sub> K	7795	2NaK→Na <sub>2</sub> K+K	+3352 (forbidden)
K <sub>2</sub> Na	7125	2NaK→K <sub>2</sub> Na+Na	+2752 (forbidden)

From this analysis, investigating the energetics of reactions involving pairs of NaK dimers in their singlet ground electronic state, it is concluded that trimer formation is always energetically forbidden for low-lying rovibrational states of the singlet dimers [53]. However, this does not exclude trimer formation for low-lying rovibrational states of heteronuclear dimers in their triplet ground state. As studied in [55], it can be shown that contrary to the case of the singlet dimer the trimer formation of triplet dimers is always energetically allowed.

---

<sup>10</sup>the energy required to form a monoatomic gaseous species

# Conclusion and outlook

With the new degenerate Bose-Fermi mixture of  $^{23}\text{Na}$  and  $^{40}\text{K}$ , and over thirty  $s$ -,  $p$ - and wave interspecies Feshbach resonances, including several exceptionally broad resonances, the future is bright (and ultracold) for Fermi 1. The strongly interacting  $^{23}\text{Na}$ - $^{40}\text{K}$  mixture near these Feshbach resonances should allow the study of Bose or Fermi polarons [56], of boson mediated interactions between fermions, and possibly of novel states of matter. Future experiments with Fermi 1 might include an optical lattice that will discriminate one species versus the other, thus making the machine even more versatile in the manipulation of parameters. Of particular interest can be to address one of the original questions that Fermi 1 set out to solve: How does adding impurities change the behaviour of a many-body-system? The physics of disorder. Looking forward to hearing about those results.

NaK molecules are already there and it is a matter of technical expertise to be able to bring them to the rovibrational ground state. NaK molecules possess a large permanent electric dipole moment and are stable against exchange collisions, all make this molecule very attractive for research. One can thus hope to create a Fermi gas of polar molecules with strong dipole-dipole interactions that dominate the many-body physics of the gas.

Fermi 1 will continue to realize fundamental models of condensed matter physics in a fully controllable environment, testing them with the precision of atomic physics and for that it has the essential tools: a very powerful, stable and versatile machine; the necessary great ideas and very capable people.



# Bibliography

- [1] Immanuel Bloch, Jean Dalibard, and Wilhelm Zwerger. Many-Body Physics with Ultracold Gases. *Reviews of Modern Physics*, 80(3):885–964, 2007.
- [2] Richard Feynman. Simulating physics with computers. *International Journal of Theoretical Physics*, 21(6):467–488, 1982.
- [3] K. B. Davis, M. O. Mewes, M. R. Andrews, N. J. van Druten, D. S. Durfee, D. M. Kurn, and W. Ketterle. Bose-Einstein Condensation in a Gas of Sodium Atoms. *Phys. Rev. Lett.*, 75:3969–3973, Nov 1995.
- [4] B. DeMarco and D.S. Jin. Onset of Fermi degeneracy in a trapped atomic gas. *Science*, 285:1703–1706, 1999.
- [5] W. Pauli. The connection between spin and statistics. *Phys. Rev.*, 58:716–722, Oct 1940.
- [6] *Quantum Liquid*. Oxford University Press, 2006.
- [7] W. Ketterle, D.S. Durfee, and D.M. Stamper-Kurn. Making, probing and understanding Bose-Einstein condensates. In M. Inguscio, S. Stringari, and C.E. Wieman, editors, *Bose-Einstein condensation in atomic gases, Proceedings of the International School of Physics Enrico Fermi, Course CXL, Varenna, 7-17 July 1998*, pages 67–176. IOS Press, Amsterdam, 1999.
- [8] W. Ketterle and M.W. Zwierlein. Making, probing and understanding ultracold Fermi gases. In M. Inguscio, W. Ketterle, and C. Salomon, editors, *Ultracold Fermi Gases, Proceedings of the International School of Physics "Enrico Fermi", Course CLXIV, Varenna, 20 - 30 June 2006*. IOS Press, Amsterdam., 2008.
- [9] Tobias Tiecke. *Feshbach resonances in ultracold mixtures of the fermionic quantum gases  $^6\text{Li}$  and  $^{40}\text{K}$* . PhD thesis, Amsterdam University, 2009.
- [10] M.E. Gehm. *Preparation of an Optically-Trapped Degenerate Fermi Gas of  $^6\text{Li}$ : Finding the Route to Degeneracy*. PhD thesis, Duke University, 2003.
- [11] William Phillips. Laser cooling and trapping of neutral atoms. *Nobel Lecture*, 1997.

- [12] Sara Campbell. *Building an Apparatus for Ultracold Lithium-Potassium Fermi-Fermi mixtures*. PhD thesis, MIT, 2010.
- [13] D. M Stamper-Kurn. *Peeking and poking at a new quantum fluid: Studies of gaseous BEC in magnetic and optical traps*. PhD thesis, MIT, 1999.
- [14] Yan Feng, Luke R. Taylor, and Domenico Bonaccini Calia. 25 W Raman-fiber-amplifier-based 589 nm laser for laser guide star. *Opt. Express*, 17(21):19021–19026, Oct 2009.
- [15] *CVI Technical Guide*. CVI Melles Griot, 2012.
- [16] *Acousto-Optics*. CRC Press, 1997.
- [17] T. W. Hänsch, I. S. Shahin, and A. L. Schawlow. High-resolution saturation spectroscopy of the sodium  $d$  lines with a pulsed tunable dye laser. *Phys. Rev. Lett.*, 27:707–710, Sep 1971.
- [18] L. De Sarlo, P. Maioli, G. Barontini, J. Catani, F. Minardi, and M. Inguscio. Collisional properties of sympathetically cooled  $^{39}\text{K}$ . *Phys. Rev. A*, 75(2):022715, 2007.
- [19] Robert L. D. Campbell, Robert P. Smith, Naaman Tammuz, Scott Beattie, Stuart Moulder, and Zoran Hadzibabic. Efficient production of large  $^{39}\text{K}$  bose-einstein condensates. *Phys. Rev. A*, 82:063611, Dec 2010.
- [20] G. Roati, M. Zaccanti, C. D’Errico, J. Catani, M. Modugno, A. Simoni, M. Inguscio, and G. Modugno.  $^{39}\text{K}$  Bose-Einstein Condensate with Tunable Interactions. *Phys. Rev. Lett.*, 99:010403, Jul 2007.
- [21] T. Kishimoto, J. Kobayashi, K. Noda, K. Aikawa, M. Ueda, and S. Inouye. Direct evaporative cooling of  $^{41}\text{K}$  into a Bose-Einstein Condensate. *Phys. Rev. A*, 79:031602, Mar 2009.
- [22] Wolfgang Ketterle and Martin W Zwierlein. Making, probing and understanding ultracold Fermi gases. *Gas di Fermi ultrafreddi*, 31(June 2006):206, 2008.
- [23] Andrew G. Truscott, Kevin E. Strecker, William I. McAlexander, Guthrie B. Partridge, and Randall G. Hulet. Observation of fermi pressure in a gas of trapped atoms. *Science*, 291(5513):2570–2572, 2001.
- [24] C. Ospelkaus, S. Ospelkaus, L. Humbert, P. Ernst, K. Sengstock, and K. Bongs. Ultracold heteronuclear molecules in a 3D optical lattice. *Phys. Rev. Lett.*, 97(12):120402, 2006.
- [25] Cheng Chin, Rudolf Grimm, Paul Julienne, and Eite Tiesinga. Feshbach resonances in ultracold gases. *Rev. Mod. Phys.*, 82(2):1225, 2010.

- [26] Cheng-Hsun Wu, Ibon Santiago, Jee Woo Park, Peyman Ahmadi, and Martin W. Zwierlein. Strongly interacting isotopic bose-fermi mixture immersed in a fermi sea. *Phys. Rev. A*, 84:011601, Jul 2011.
- [27] Jee Woo Park, Cheng-Hsun Wu, Ibon Santiago, Tobias G. Tiecke, Sebastian Will, Peyman Ahmadi, and Martin W. Zwierlein. Quantum degenerate bose-fermi mixture of chemically different atomic species with widely tunable interactions. *Phys. Rev. A*, 85:051602, May 2012.
- [28] Wolfgang Demtröder. *An Introduction to Atomic and Molecular Physics*. Springer, 2011.
- [29] A. Gerdès, M. Hobein, H. Knöckel, and E. Tiemann. Ground state potentials of the NaK molecule. *The European Physical Journal D*, 49(1):67–73, July 2008.
- [30] John Weiner, Vanderlei S. Bagnato, Sergio Zilio, and Paul S. Julienne. Experiments and theory in cold and ultracold collisions. *Rev. Mod. Phys.*, 71:1, 1999.
- [31] T. Tiecke, M. Goosen, J. Walraven, and S. Kokkelmans. Asymptotic-bound-state model for Feshbach resonances. *Physical Review A*, 82(4), October 2010.
- [32] Cheng Chin, Paul Julienne, and Eite Tiesinga. Feshbach resonances in ultracold gases. *Reviews of Modern Physics*, 82(2):1225–1286, 2010.
- [33] C. Ticknor, C. A. Regal, D. S. Jin, and J. L. Bohn. Multiplet structure of Feshbach resonances in nonzero partial waves. *Phys. Rev. A*, 69:042712, 2004.
- [34] Thomas M. Hanna, Eite Tiesinga, and Paul S. Julienne. Prediction of feshbach resonances from three input parameters. *Phys. Rev. A*, 79:040701, Apr 2009.
- [35] A. Gerdès, M. Hobein, H. Knckel, and E. Tiemann. Ground state potentials of the nak molecule. *Eur. Phys. J. D*, 49(1):67–73, 2008.
- [36] Francesca Ferlaino, Chiara D’Errico, Giacomo Roati, Matteo Zaccanti, Massimo Inguscio, Giovanni Modugno, and Andrea Simoni. Feshbach spectroscopy of a k-rb atomic mixture. *Phys. Rev. A*, 73(4):040702, 2006.
- [37] Richard Willstätter. On plant pigments. In *Nobel Lecture, June 3, 1920*.
- [38] Amedeo Avogadro. Note sur la nécessité de distinguer les molécules intégrantes des corps de leurs équivalents chimiques. *Archives des sciences physiques et naturelles, Volumes 10-12*, 1849.
- [39] J. B. Perrin. Mouvement brownien et réalité moléculaire. *Annales de chimie et de physique VIII* 18, 5-114, 1909.
- [40] Wolfgang Demtröeder. *Molecular Physics: Theoretical Principles and Experimental Methods*. WILEY-VCH Verlag GmbH & Co. KGaA, 2005.

- [41] V Bednarska et al. A three-section heat-pipe oven for heteronuclear alkali molecules. *Meas. Sci. Technol.* 7, 1996.
- [42] Oppenheimer JR. Born M. Zur quantentheorie der moleküle. *Ann Phys (Leipzig)*, 1927.
- [43] S Magnier, M Aubert-Frécon, and P Millie. Potential Energies, Permanent and Transition Dipole Moments for Numerous Electronic Excited States of NaK. *Journal of molecular spectroscopy*, 200(1):96–103, March 2000.
- [44] Russier-Antoine et al. An improved potential energy curve for the ground state of nak. *J. Phys. B: At. Mol. Opt. Phys.*, 2000.
- [45] Robert J. Leroy and Richard B. Bernstein. Dissociation energies of diatomic moleculles from vibrational spacings of higher levels: application to the halogens\*. *Chemical Physics Letters*, 5(1):42–44, February 1970.
- [46] B. J. Verhaar, E. G. M. van Kempen, and S. J. J. M. F. Kokkelmans. Predicting scattering properties of ultracold atoms: Adiabatic accumulated phase method and mass scaling. *Physical Review A*, 79(3), March 2009.
- [47] A. Derevianko, J. F. Babb, and A. Dalgarno. High-precision calculations of van der waals coefficients for heteronuclear alkali-metal dimers. *Phys. Rev. A*, 63(5):052704, 2001.
- [48] G. Gribakin and V. Flambaum. Calculation of the scattering length in atomic collisions using the semiclassical approximation. *Physical Review A*, 48(1):546–553, July 1993.
- [49] Harald Friedrich and Patrick Raab. Near-threshold quantization and scattering lengths. *Physical Review A*, 77(1), January 2008.
- [50] Goulven Quéméner and John L. Bohn. Strong dependence of ultracold chemical rates on electric dipole moments. *Phys. Rev. A*, 81:022702, Feb 2010.
- [51] S. Knoop, T. Schuster, R. Scelle, A. Trautmann, J. Appmeier, M. Oberthaler, E. Tiesinga, and E. Tiemann. Feshbach spectroscopy and analysis of the interaction potentials of ultracold sodium. *Physical Review A*, 83(4), April 2011.
- [52] A Pashov, P Popov, H Knöckel, and E Tiemann. Spectroscopy of the  $a^3\Sigma_u^+$  state and the coupling to the  $X^1\Sigma_g^+$  state of  $K_2$ . *The European Physical Journal D*, 46(2):241–249, 2007.
- [53] Piotr uchowski and Jeremy Hutson. Reactions of ultracold alkali-metal dimers. *Physical Review A*, 81(6):060703, 2010.
- [54] D. Pavolini and F. Spiegelmann. Ab initio ground state properties of neutral  $X_2Y$  and ionic  $X_2Y^+$  ( $X,Y=Li, Na, K$ ) alkali trimers. *The Journal of Chemical Physics*, 87(5):2854, September 1987.

- [55] Pavel Soldán. Lowest quartet states of heteronuclear alkali-metal trimers. *Physical Review A*, 82(3), September 2010.
- [56] Andre Schirotzek, Cheng-Hsun Wu, Ariel Sommer, and Martin W. Zwierlein. Observation of fermi polarons in a tunable fermi liquid of ultracold atoms. *Phys. Rev. Lett.*, 102(23):230402–4, 2009.